Response to reviews of "Why increased extreme precipitation under climate change negatively affects water security" submitted to *Hydrology and Earth System Sciences* for consideration for publication.

Editor comments

Based on the last referees' appraisals on your revised manuscript and before its final acceptance, I believe that some clarifications are still required with specific reference to the equation you used to model the infiltration excess mechanism. I refer to Lines 13-14 at Page 4 where you state that "The model simulates infiltration excess surface runoff based on the Green-Ampt formula (Heber Green and Ampt, 1911).", and consequently to your Eq.(S1). In the supplement document your state that this equation (S1) "… is inspired by the Green-Ampt formula (Heber Green and Ampt, 1911)".

I refer to the classic Green-Ampt (GA) infiltration equation [for a uniform soil profile and assuming that matric pressure head at the soil surface is near zero (i.e. no ponding, but full saturation)] that can be written as follows:

$$q_0(t) = \left[1 + \frac{\Delta\theta|h_f|}{I(t)}\right]$$

where q_0 is infiltration rate [flux density of water across the soil surface ($z=0$)], $\Delta\theta = (\theta_{sat} - \theta_{in})$ is soil-water content deficit, with θ_{in} the initial soil-water content in the uniform soil profile (soil moisture, for short), and $I(t)$ is cumulative infiltration.

> *Thank you for your concerns regarding Eq. S1. First of all, Eq. S1 was developed to overcome the limitations and restriction of existing infiltration equations. The curve number method is often applied at daily time steps, but we argue that this method has its limitations regarding the interpretation of the hydrologic soil groups and hydrologic conditions. Therefore, we developed a new equation that can be applied at a daily time step and, while simplified and not equal to, was mostly inspired by the Green-Ampt equation. Due to data limitations, especially for large-scale assessments, and due to the daily time step of our assessments, we decided to deviate from the Green-Ampt equation. We recognize the concerns that you have raised, for which we provided a point-by-point response below.*

If one compares the classic GA equation with your Eq.(S1), one may note the following:

a) Eq.(S1) sets a soil-water content deficit as ($\theta_{sat} - \theta$), with θ the actual soil-water content during your simulations (if I am right), whereas the GA equation employs the term ($\theta_{sat} - \theta_{in}$), with θ_{in} the initial soil-water content in the uniform soil profile (soil moisture, for short). At Page 6, Eq.(1), you state that θ is soil moisture at time step *t*. Is this soil moisture meaning the same in both equations (1) and (S1)?

> *The soil water content from Eq. (1) and (S1) are not equal and are acquired at a different moment within the model routine. The soil water content from Eq. (S1) is equal to the soil moisture content of the previous time step, which represents the initial soil water content from the Green-Ampt equation. The soil water content from Eq. (1) is equal to the soil moisture content after water infiltrates into the soil. We have clarified this in the main manuscript and Supporting Information.*

b) In the brackets of the right-hand side of the classic GA equation, there appears the matric suction head at the wetting front (h_f). This term is very important for modeling an infiltration event, but it does not even appear in your Eq.(S1). One may wonder what are the implications of this choice especially in terms of deviations from the classic GA equation? Actually, it might be also interesting to ascertain the implications of this choice with respect to an infiltration process simulated by the Richards equation.

> *Indeed, we did not include the matric suction head at the wetting front (h_f) in Eq. S1. The main reason for this deviation is that data (e.g. soil porosity) that is required to determine the matric suction head at the wetting front is most often not available at the spatial scale the model is applied. Instead, we divide the soil water content deficit by θ_{sat} to account for the hydraulic properties of the soil and to account for the dimensions of the fraction between the brackets of the right-hand side of the equation, which is dimensionless in the Green-Ampt equation. While this is indeed a simplification as compared to the GA equation, we consider this reasonable for assessments with a daily time step and for large study areas with a coarse spatial resolution.*

c) Moreover, in the brackets of the right-hand side of the classic GA equation, at the denominator of the soil-water content deficit, there appears the cumulative infiltration [$I(t)$]. In your Eq.(S1) there is only the saturated soil-water content. A clear explanation of this choice is required to the benefit of wider readership.

> *The Green-Ampt equation is applied at a sub-daily time step, hence, the cumulative infiltration ($I(t)$) can be calculated from the subsequent time steps. However, since our infiltration equation is applied at a daily time step, the cumulative infiltration at a sub-daily time step cannot be determined. The cumulative infiltration causes the Green-Ampt equation to behave non-linear over time. To account for this non-linear behaviour, we included the calibration parameter λ, which we discussed in more detail below.*

d) Using Bouwer's approximation ($K_{eff} \approx 0.5\ K_{sat}$) might not be appropriate in the case of your Eq.(S1) since this equation differs (quite a lot, I guess) from the classic GA equation. Please, give adequate justifications for your choice.

> *Indeed, especially the right-hand side of the Green-Ampt equation differs from our infiltration equation, see previous and next comments. The left-hand side of both the Green-Ampt and Eq. (S1) consists of the effective hydraulic conductivity, which can be obtained from a range of different methods. Brouwer's approximation is probably one of the most straightforward methods available and requires the saturated hydraulic conductivity, which is readily available from the SPHY-MMF model. Other methods require more data, such as the curve number (Nearing et al., 1996) or information on coarse rock fragments, frozen soil, soil crusting and soil macroporosity (Rawls et al., 1989). Hence, the choice for this approximation was mostly data driven.*

Finally, additional and more in-depth information is required about the exponent λ. You state that it is a calibration parameter. Information is required about what soil properties mainly affect this parameter and how you have calibrated it in the present study.

We have included this calibration parameter to account for the non-linearity of infiltration. A similar calibration parameter is also included in the infiltration capacity equation of the VIC hydrological model (i.e. infiltration shape parameter). In the current manuscript, we set this parameter to a value of 0.25 and did not use it to calibrate the model.

To summarize, we replaced the fraction h_f / I(t) from the Green-Ampt equation by 1 / θ_{sat}. We divide by θ_{sat} to account for the differences in soil properties, which are originally expressed by the matric suction head at the wetting front (h_f). The cumulative infiltration in the Green-Ampt equation reduces the infiltration capacity in each subsequent time step. To account for this non-linear behaviour, we included the calibration parameter λ. These deviations from the Green-Ampt equation certainly have implications for the validity of the equation. We acknowledge that it would be interesting to compare the full Green-Ampt equation with our equation, most certainly in combination with measured infiltration rates from field experiments and sub-daily time steps. By doing so, we can establish the sensitivity of the model parameters, such as the calibration parameter λ and the approximation of the effective hydraulic conductivity. We do think that this is beyond the objective of the current study though.

We have included the following sentences to the Supporting information, to clarify our deviations from the original Green-Ampt equation:
"Equation S1 deviates for some aspects from the original Green-Ampt equation. The soil moisture content θ is the soil moisture content of the previous time step. We divide by θ_{sat} to account for the differences in soil properties, which are originally expressed by the matric suction head at the wetting front. The cumulative infiltration in the Green-Ampt equation reduces the infiltration capacity in each subsequent time step. To account for this non-linear behaviour, we included the calibration parameter λ. This simplification of the Green-Ampt equation is considered justified for assessments with a daily time step and for large study areas with a coarse spatial resolution."

Furthermore, we changed the following sentence in the main manuscript (Lines 13-14 at Page 4):
"The model simulates infiltration excess surface runoff based on an adaptation of the Green-Ampt equation (Heber Green and Ampt, 1911)."

References
Rawls, W.J., J.J. Stone, and D.L. Brakensiek. 1989. Chapter 4; Infiltration. In: L.J. Lane and M.A. Nearing (eds.), Profile Model Documentation. USDA-Water Erosion Prediction Project: Hillslope Profile Version. NSERL Report No. 2, USDA-ARS, National Soil Erosion Research Lab., W, Lafayette, Ind.

Nearing, M.A., B.Y. Liu, L.M. Risse, and X. Zhang. 1996. Curve number and Green-Ampt effective hydraulic conductivities. Water Resources Bulletin 32:125-136.

List of all relevant changes made in the manuscript

- Revised a sentence in the Model Description where we refer to the Green-Ampt equation in the main document.
- Explained which soil moisture content we use in Eq. (1) in the main document.
- Explained which soil moisture content we use in Eq. (S1) in the Supporting Information.
- Added a discussion on the differences between Eq. (S1) and the Green-Ampt equation in the Supporting Information.

Why increased extreme precipitation under climate change negatively affects water security

Joris P.C. Eekhout[1], Johannes E. Hunink[2], Wilco Terink[3], and Joris de Vente[1]

[1]Soil Erosion and Conservation Research Group, CEBAS-CSIC, Spanish Research Council, Campus Universitario Espinardo, 30100, P.O. Box 164, Murcia, Spain
[2]FutureWater, Calle San Diego 17 4a, 30202, Cartagena, Spain
[3]FutureWater, Costerweg 1V, 6702 AA, Wageningen, The Netherlands

Correspondence: Joris Eekhout (joriseekhout@gmail.com)

Abstract. An increase of extreme precipitation is projected for many areas worldwide in the coming decades. To assess the impact of increased precipitation intensity on water security, we applied a regional scale hydrological and soil erosion model, forced with Regional Climate Model projections. We specifically considered the impact of climate change on the distribution of water between soil (green water) and surface water (blue water) compartments. We show that an increase in precipitation intensity leads to a redistribution of water within the catchment, where water storage in soil decreases and reservoir inflow increases. This affects plant water stress and the potential of rainfed versus irrigated agriculture, and increases dependency on reservoir storage, that is potentially threatened by increased soil erosion. This study demonstrates the crucial importance of accounting for the fact that increased precipitation intensity leads to water redistribution between green and blue water, increased soil erosion, and reduced water security. Ultimately, this has implications for design of climate change adaptation measures, which should aim to increase the water holding capacity of the soil (green water) and to maintain the storage capacity of reservoirs (blue water), benefiting rainfed and irrigated agriculture.

Copyright statement. TEXT

1 Introduction

For many areas worldwide, increased rainfall intensity and frequency of extreme weather events are projected for the coming decades (Sun et al., 2007; O'Gorman and Schneider, 2009; Sillmann et al., 2013). Yet, there is surprisingly little known about how this will affect water security at regional scales, most relevant for policy making (Nicholson et al., 2009). Water security is defined as a condition in which the population has access to adequate quantities of clean water to sustain livelihoods and is protected against water related disasters (UN-Water, 2013). Accurate quantification of the impacts of climate change on water security is crucial for the design and evaluation of effective adaptation strategies and implementation of the Sustainable Development Goals (SDGs; United Nations General Assembly, 2015), in particular SDG 6 (clean water and sanitation), SDG 13 (climate action) and SDG 15 (life on land). Previous impact studies have indicated how climate change may affect water

availability, flood risk (Sperna Weiland et al., 2012; Arnell and Gosling, 2013; Forzieri et al., 2014; Donnelly et al., 2017; Thober et al., 2018) and soil erosion (Li and Fang, 2016), with positive and negative reported impacts. However, these estimates insufficiently account for actual impacts on the redistribution of water between soil and surface water compartments. While water storage potential in soils (green water) and reservoirs (blue water) is increasingly important for climate change adaptation, there is insufficient knowledge of how both are affected by increasing precipitation intensity and how this affects crucial aspects of water security such as plant water stress, reservoir inflow, soil erosion and reservoir storage potential.

The expected increase of extreme precipitation will have multiple impacts on urban, natural and arable environments, and may for example cause increased flood frequency (e.g. Thober et al., 2018). However, as a result of increased temperature and, consequently, increased evapotranspiration, antecedent soil moisture conditions may change and affect the impact of increased flood magnitude (Castillo et al., 2003; Ivancic and Shaw, 2015; Wasko and Sharma, 2017). In urban areas, an increase of extreme precipitation may affect inundation frequency and may pose challenges for stormwater infrastructure, which is often designed under the assumption of a stationary climate (Mishra et al., 2012). In natural environments, a combination of an increase of extreme precipitation and longer dry spells may cause an increase stress conditions for natural vegetation (Fay et al., 2003; Knapp et al., 2008; León-Sánchez et al., 2018). Rainfall intensity is one of the main drivers for soil erosion (Nearing et al., 1990) and is one of the dominant processes that may affect soil erosion under future climate conditions (Nearing et al., 2004). In fact, both runoff and soil erosion are among the processes most sensitive to changes in rainfall intensity (Pruski and Nearing, 2002; Nunes et al., 2009b). Soil erosion of arable land and related loss of organic matter and nutrients is a major threat for agricultural productivity, which is already under pressure by increasing food demands (Pimentel et al., 1995).

Hydrological and soil erosion studies on the impact of climate change are generally forced with future projected climate data from Global Circulation Models (GCMs). To enhance accuracy and spatial resolution of climate projections some studies adopt Regional Climate Models (RCMs) to downscale GCM output (Jacob et al., 2014) and apply bias-correction methods to overcome the bias between historical observed and modelled data. While the change factor (or delta change) approach is the most popular bias-correction method, other bias-correction methods that consider the change in future precipitation distribution are needed to assess the effects of changes in frequency and intensity of extreme events (Mullan et al., 2012; Li and Fang, 2016). The selection of climate models, downscaling and bias-correction methods strongly affects the climate projections (Maraun et al., 2017) and consequently also the simulated hydrological and erosional response. Moreover, most global and regional studies only consider saturation excess surface runoff and disregard infiltration excess surface runoff, which may lead to an underestimation of the actual impact of extreme precipitation on surface runoff generation. Saturation excess and infiltration excess are the main mechanisms causing surface runoff. They may co-exist within a catchment and occur at different times or places due to differences in spatio-temporal conditions, i.e. antecedent soil moisture, soil characteristics or precipitation intensities (Beven, 2012). Infiltration excess surface runoff is mainly driven by precipitation intensity and is responsible for major parts of surface runoff generation in many parts of the world, such as the Mediterranean (Merheb et al., 2016; Manus et al., 2008) and semi-arid environments (Lesschen et al., 2009; García-Ruiz et al., 2013), due to steep slopes, low infiltration rates and frequent intense precipitation events. Considering the estimated future increase of extreme precipitation in many regions, infiltration excess surface runoff will become increasingly more important.

Climate change will affect soil erosion through changes in precipitation volume and intensity and through climate change induced changes in vegetation cover. Climate change induced increase in extreme precipitation is likely to be a dominant factor causing future increase of soil erosion (Nearing et al., 2004; Nunes et al., 2008), as was demonstrated in various hillslope scale (Zhang et al., 2012; Mullan et al., 2012; Routschek et al., 2014) and catchment-scale event-based model studies (Baartman et al., 2012; Paroissien et al., 2015). Given the relevance of precipitation intensity, appropriate bias-correction methods and accounting for infiltration excess surface runoff are particularly important to assess the impact of climate change. However, large-scale assessments rarely consider the impact of increased extreme precipitation frequency on soil erosion rates. They are either applied at a low temporal resolution (e.g. monthly time steps), hence, focusing on changes in precipitation volume, or use bias-correction methods that do not consider changes in the frequency distribution (e.g. the delta change method), leading to strong underestimation of the impact of climate change. Furthermore, vegetation cover mitigates soil erosion through canopy interception and flow resistance (Nearing et al., 2004; Nunes et al., 2013). However, the interactions between reduced precipitation, increased temperature and changes in the vegetation cover are rarely assessed in soil erosion impact studies, while the change in vegetation cover may have a significant impact on hydrological and soil erosion processes (Nunes et al., 2009a).

Due to the inherent nature of the processes involved, such as infiltration excess surface runoff and soil erosion, the impact of extreme precipitation can only be assessed at a sufficiently detailed spatial and temporal scale. Therefore, the objective of this study was to examine the effect of climate change on water security through application of a spatially-distributed hydrological model (SPHY; Terink et al., 2015), coupled with a soil erosion model (MMF; Morgan and Duzant, 2008), that runs at a daily time step. The hydrological model simulates the main hydrological processes, including infiltration excess surface runoff. The model was applied to the Segura River catchment, a typical large Mediterranean river catchment, highly regulated by reservoirs. We applied the model to a reference scenario and 4 future climate scenarios, where we accounted for the multiple effects of climate change, including precipitation intensity, and seasonal and inter-annual vegetation development.

2 Material & Methods

2.1 Study Area

The study is performed in the Segura River catchment in the southeast of Spain (Fig. 1). The catchment area covers 15,978 km^2 and has an elevation ranging between sea level and 2055 m.a.s.l. (Fig. 1c). The climate in the catchment is classified as Mediterranean (Csa according to the Köppen-Geiger climate classification) in the headwaters (19%) and semi-arid (BSk) in the rest of the catchment (81%). Catchment-averaged mean annual precipitation amounts to 361 mm (for the period 1981-2000) and mean annual temperature ranges between 9.3 and 18.7 °C (1981-2000) in the headwaters and downstream area, respectively.

The main landuse types are shrubland (28%), forest (26%), cereal fields (14%) and almond orchards (9%) (Fig. 1d). Agriculture accounts for 44% of the catchments surface area and can be subdivided into rainfed crops (31%; cereal fields, almond orchards, vineyards and olive orchards), irrigated crops (12%; fruit trees and horticulture) and other agriculture (1%). The main

soil classes are Calcisols (41%), Leptosols (35%), Luvisols (4%) and Kastanozems (4%) (Fig. 1e). There are 33 reservoirs in the catchment, from which 14 are allocated exclusively for irrigation purposes (Fig. 1b and Table S2) with a total capacity of 866 Hm^3. The other reservoirs have mixed functions for electricity supply and flood prevention. Besides reservoirs, irrigation water demand is also met with water from deep aquifers and the Tagus-Segura water transfer. These additional water sources

5   and the supply of water to irrigated agriculture are not accounted for in this study, not in the least because there is high uncertainty regarding the spatial and temporal variation of irrigated agriculture and reservoir operation. This means that our results on water availability include water available for irrigation purposes, irrespective of reservoir operation.

2.2   Model Description

We applied the spatially-distributed Spatial Processes in HYdrology model (SPHY; Terink et al., 2015), coupled with the

10 Morgan-Morgan-Finney soil erosion model (MMF; Morgan and Duzant, 2008), described in detail in Eekhout et al. (2018). The hydrological model simulates the most relevant hydrological processes, such as interception, evapotranspiration, dynamic evolution of vegetation cover, including seasonal patterns and response to climate change, surface runoff, and lateral and vertical soil moisture flow at a daily ~~timestep~~time step, here implemented at 200 m spatial resolution. The model simulates infiltration excess surface runoff based on an adaptation of the Green-Ampt ~~formula~~ equation (Heber Green and Ampt, 1911).

15 The soil erosion model is based on the MMF model (Morgan and Duzant, 2008), runs at a daily ~~time-step~~ time step and is fully coupled with the hydrological model. Soil detachment is determined as a function of raindrop impact and accumulated runoff. In-field deposition is a function of the abundance of vegetation and soil roughness. The remainder will go into transport, considering the transport capacity of the flow and a sediment trapping formula to account for the deposition of sediment in reservoirs. The model incorporates a vegetation module that considers inter- and intra-annual vegetation development and

20 provides vegetation input to both the hydrological and the soil erosion model (see SI and Eekhout et al. (2018) for a detailed description of the model, input data and calibration).

2.3   Climate scenarios

We applied four different future climate scenarios, divided over two future periods (i.e. 2031-2050 and 2081-2100) and two Representative Concentration Pathways (i.e. RCP4.5 and RCP8.5), describing an emission scenario peaking in 2040 followed

25 by a decline (RCP4.5) and an emission scenario with continuous increase of emissions throughout the 21st century (RCP8.5). We obtained data from a total of nine climate models (Table S3) from the EURO-CORDEX initiative (Jacob et al., 2014), with a 0.11° resolution. Quantile mapping has been recognized as the empirical-statistical downscaling and bias-correction method that shows the best performance, particularly for the highest quantiles (Themeßl et al., 2011). Changes in extreme precipitation may have a large impact on the hydrological and soil erosion processes, therefore, quantile mapping was selected

30 for the current study. Quantile mapping first determines the probability of occurrence of the future precipitation from the empirical cumulative density distribution function (ecdf) of the historical climate model output. Then a correction factor is determined by feeding this probability into the inverse ecdfs of the historical observed and historical climate model output. Finally, the correction factor is added to the future precipitation. We adopted the method proposed by Themeßl et al. (2012)
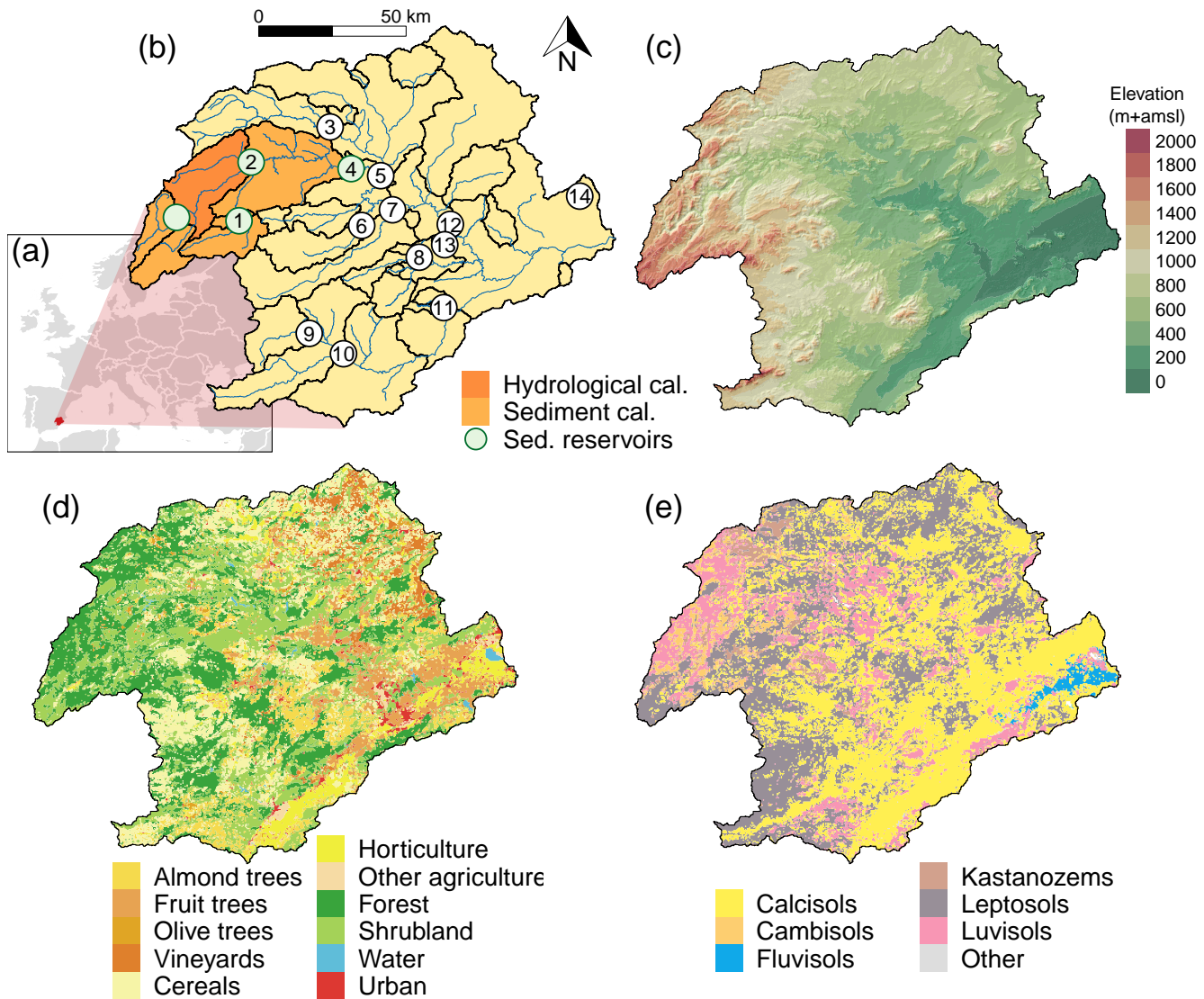
Figure 1. Location and characteristics of the Segura River catchment: (a) location of the catchment within Europe, (b) location of the subcatchments (yellow), the hydrological calibration area (dark orange), the soil erosion calibration area (light orange), the channels (blue), the reservoirs (numbers 1-14), and the calibration reservoirs (green dots), (c) Digital Elevation Model (Farr et al., 2007), (d) landuse map (MAPAMA, 2010), and (e) soil classification map (Hengl et al., 2017).

that accounts for the dry-day frequency, which could lead to uncertainties when the dry-day frequency of the historical climate model output is greater than in the historical observations. Furthermore, this method accounts for new extremes, to correct for new extreme precipitation values that do not occur in the historical observations. Daily precipitation and temperature data for the reference scenario (1981-2000) were, respectively, obtained from the SPREAD dataset (Serrano-Notivoli et al., 2017),

with a 5 km resolution, and the SPAIN02 dataset (Herrera et al., 2016), with a 0.11° resolution. The model simulations were performed consecutively and included one start-up year, which was sufficient to reach a dynamic equilibrium state for storage components (e.g. soil moisture compartments and reservoir storage).

2.4 Water Security Indicators

5 We evaluated the impact of climate change on water security using plant water stress, reservoir inflow, hillslope erosion and reservoir sediment yield as impact indicators. These indicators are specifically important for this study area, which is dominated by rainfed and irrigated agriculture. Changes in plant water stress and hillslope erosion may affect agricultural productivity, while changes in reservoir inflow and reservoir sediment yield affect water availability for irrigated agriculture and drinking water.

10 Plant water stress, defined as an indicator between no stress (0) and fully stressed (1), was determined by comparing the soil moisture content in the root layer with the plant specific soil moisture content from which stress starts to occur and soil moisture at wilting point. Plant water stress is determined using the following equation (adapted from Porporato et al., 2001)):

$$\mathrm{PWS} = \frac{\theta_{\mathrm{PWS}} - \theta(t)}{\theta_{\mathrm{PWS}} - \theta_{\mathrm{PWP}}} \tag{1}$$

where PWS is the dimensionless plant water stress, $\theta(t)$ is the soil moisture content at ~~timestep~~ time step t after water has
15 infiltrated into the soil, θ_{PWS} is the plant and soil specific soil moisture content from which plant water stress starts to occur and θ_{PWP} is the soil moisture content at permanent wilting point. PWS equals zero when $\theta(t) > \theta_{\mathrm{PWP}}$. The value of θ_{PWS} is determined as follows (adapted from Allen et al., 1998):

$$\theta_{\mathrm{PWS}} = \theta_{\mathrm{FC}} - d(\theta_{\mathrm{FC}} - \theta_{\mathrm{PWP}}) \tag{2}$$

where θ_{FC} is the soil moisture content at field capacity, and d is the depletion fraction. The depletion fraction is a plant specific
20 factor and is a function of the potential evapotranspiration (Allen et al., 1998):

$$d = d_{\mathrm{tab}} + 0.04(5 - ET_{\mathrm{P}}) \tag{3}$$

where d_{tab} is the tabular value of the depletion fraction and ET_{P} is the potential evapotranspiration obtained from the hydrological model. Values for d_{tab} were obtained from Allen et al. (1998). Allen et al. (1998) mainly focusses on agricultural crops. For natural vegetation, we adopted values for vegetation types that are most closely related to natural vegetation, i.e. conifer
25 trees for forest and grazing pasture for shrubland.

Reservoir inflow of the 14 reservoirs used for irrigation is defined as the cumulative discharge sum in the upstream area of a reservoir. In this calculation, only the area is considered that belongs to one reservoir. If the upstream area of a reservoir contains one or more other reservoirs, the discharge originating from these areas is omitted. Reservoir inflow is used to infer the impact on irrigation water demand. Hillslope erosion was determined from the long-term average soil erosion map. Per subcatchment
30 we determined the average of all the cells with an upstream area smaller than $10~\mathrm{km}^2$, representing hillslope erosion. Reservoir sediment yield was determined from the sediment yield timeseries obtained at each reservoir. Per reservoir we determined the

average yearly sediment yield. From reservoir sediment yield we determined annual capacity loss, by dividing the reservoir sediment yield by the storage capacity of the reservoir.

2.5 Uncertainty Analysis

To account for uncertainty we evaluated the robustness and significance of the climate projections and the model predictions within the climate model ensemble of 9 climate models. This only reflects climate model uncertainty, not the uncertainty related to other sources, such as the SPHY-MMF model. Robustness is defined as the agreement of the simulations in terms of the direction of change, i.e. changes in which more than 66% of the models agree in the direction of change were called robust changes. A paired U-test (Mann–Whitney–Wilcoxon test, with a significance level of 0.05) was applied to test the significance of model outcomes for the 9 climate models. The pairs consisted of the model output for (1) the reference scenario and (2) the 9 climate models. The paired U-test is also applied to determine the significance of the catchment-averaged change with respect to the reference scenario.

3 Results

3.1 Climate Change Signal

The future climate scenarios predict a significant 20-135 mm decrease of annual precipitation in the headwaters of the catchment, corresponding to a decrease of 3 to 24%, with respect to the reference scenario (Fig. 2 (upper row) and 3). Scenario S4 predicts significant decreases in the entire catchment, with a catchment-average decrease of 18% ($p<0.01$). All future scenarios show a robust and significant increase of annual average temperature, with changes from 1.2 $^\circ$C (scenario S1) to 3.9 $^\circ$C (scenario S4) (Fig. 3 and S3).

Changes in the intensity and frequency of precipitation may be the most relevant climate signal affecting water security, which we assessed through the intensity of extreme precipitation and the duration of dry spells. Extreme precipitation is defined as the 95th percentile of daily precipitation, considering only rainy days (>1 mm day^{-1}; Jacob et al., 2014)). Dry spells are defined as the 95th percentile of the duration of periods of at least 5 consecutive days with daily precipitation below 1 mm (Jacob et al., 2014). Under future climate conditions, extreme precipitation is likely to increase significantly in almost the entire catchment, with largest increases found for scenario S4 (Fig. 2 (lower row) and 3). The duration of dry spells is likely to significantly increase by 7-9 days (catchment-average, $p<0.02$) for scenarios S1-3 and by 26 days for scenario S4 ($p<0.01$) (Fig. 3 and S4). These results suggest a significant decrease of precipitation frequency in all 4 scenarios.

3.2 Impact on Water Security

In the reference scenario, water availability shows a distinct seasonal pattern (Fig. 4, S6 and S8). Reservoir inflow peaks in the autumn and winter months. The total annual reservoir inflow equals 400 Hm^3, which is 46% of the total capacity of the fourteen reservoirs used for irrigation. In the autumn and winter months, the plant water stress is low, except in the downstream
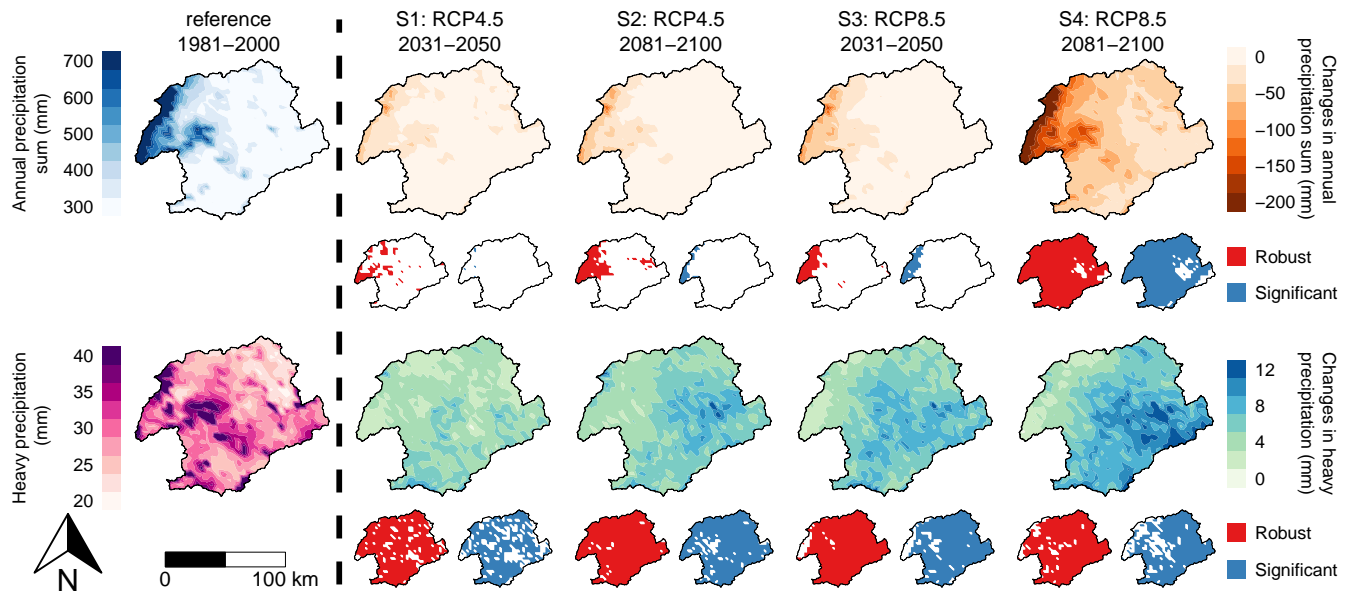
Figure 2. Ensemble average annual precipitation sum (mm, upper row) and ensemble average heavy precipitation (mm, lower row) defined as the 95th percentile of daily precipitation, considering only rainy days ($>1\,\mathrm{mm\,day^{-1}}$; Jacob et al., 2014)), for the reference scenario (left) and changes between the reference scenario and the four future scenarios (right).

part of the catchment. In the spring and more pronounced in the summer, reservoir inflow decreases and plant water stress increases. Plant water stress reaches a maximum in the summer, where the catchment-average equals 0.88.

Changes in water availability under future climate conditions show a seasonal pattern as well. In the winter months (DJF) the catchment-total reservoir inflow decreases in all scenarios, up to 36% (p<0.01) in scenario S4. Significant changes in plant water stress are projected for scenarios S2-S4 showing a catchment-average increase of 0.04 (p=0.03) to 0.11 (p<0.01). In contrast, reservoir inflow in spring (MAM) increases in all scenarios, most markedly in scenario S3 with an increase of 85% (p=0.07). A small increase in plant water stress is observed in scenarios S1-3, however, scenario S4 shows a significant catchment-average increase of 0.09 (p<0.01).

Similar results are projected for the summer months, with significant changes in plant water stress in scenario S4, showing a catchment-average increase of 0.04 (p<0.01). Surprisingly, despite of the decreasing annual precipitation, in the summer months (JJA) reservoir inflow increases, with a maximum of 119% (scenario S3, p=0.01). In the autumn months (SON) catchment-average plant water stress increases most of all seasons, ranging from 0.05 to 0.11 (p<0.01). In autumn, reservoir inflow increases in all scenarios, with a maximum of 37% (scenario S2, p=0.16). Overall, a significant yearly increase of reservoir inflow is projected for scenarios S1-3, with a maximum in scenario S3 of 28% (p<0.01) with respect to the reference scenario (Table S4). The yearly catchment-average plant water stress increases significantly in all scenarios (p<0.01), ranging from 0.03 (scenario S1) to 0.09 (scenario S4), equivalent to a 5-14% increase (Table S4).
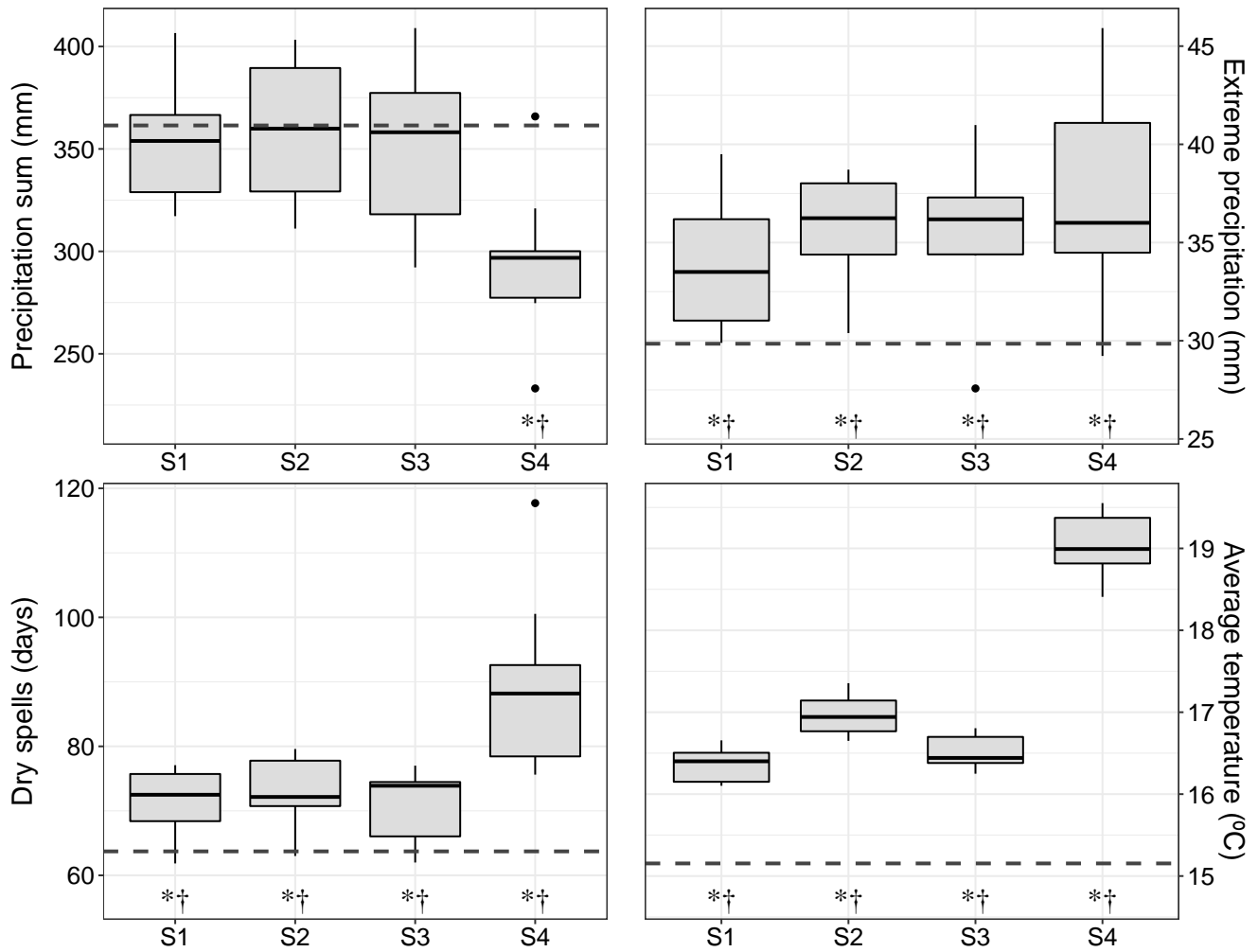
Figure 3. Catchment-average climate signal indicators, i.e. precipitation sum (mm), extreme precipitation (mm), dry spells (days) and average temperature (°C). The boxplots indicate the spread of the catchment-average among the nine climate models. In each panel the horizontal dashed line represents the catchment-average value for the reference scenario. An asterisk (∗) indicates a robust change and a dagger (†) indicates a significant change (p<0.05). The hinges indicate the 25th and 75th percentiles, the thick horizontal line indicates the median, the whiskers indicate 1.5 times the inter quantile range from each of the two hinges and the dots indicate outliers.

To understand water security and assess the potential for climate change adaptation, it is important to consider water storage capacity in reservoirs, and storage capacity loss due to soil erosion. In the reference scenario, reservoir sediment yield (SY) corresponds to a total annual capacity loss of 0.11% (Fig. 5 and S9). The average hillslope erosion (SSY) in the subcatchments ranges between 129 and 622 $\mathrm{Mg\,km^{-2}\,yr^{-1}}$. Under future climate conditions, an increase of hillslope erosion is observed in all
5   scenarios (S1-4). Hillslope erosion mainly increases in the central and downstream located subcatchments. In the headwaters, hillslope erosion decreases due to a decrease of annual precipitation (Fig. 2) and an increase in vegetation cover (Fig. S5).
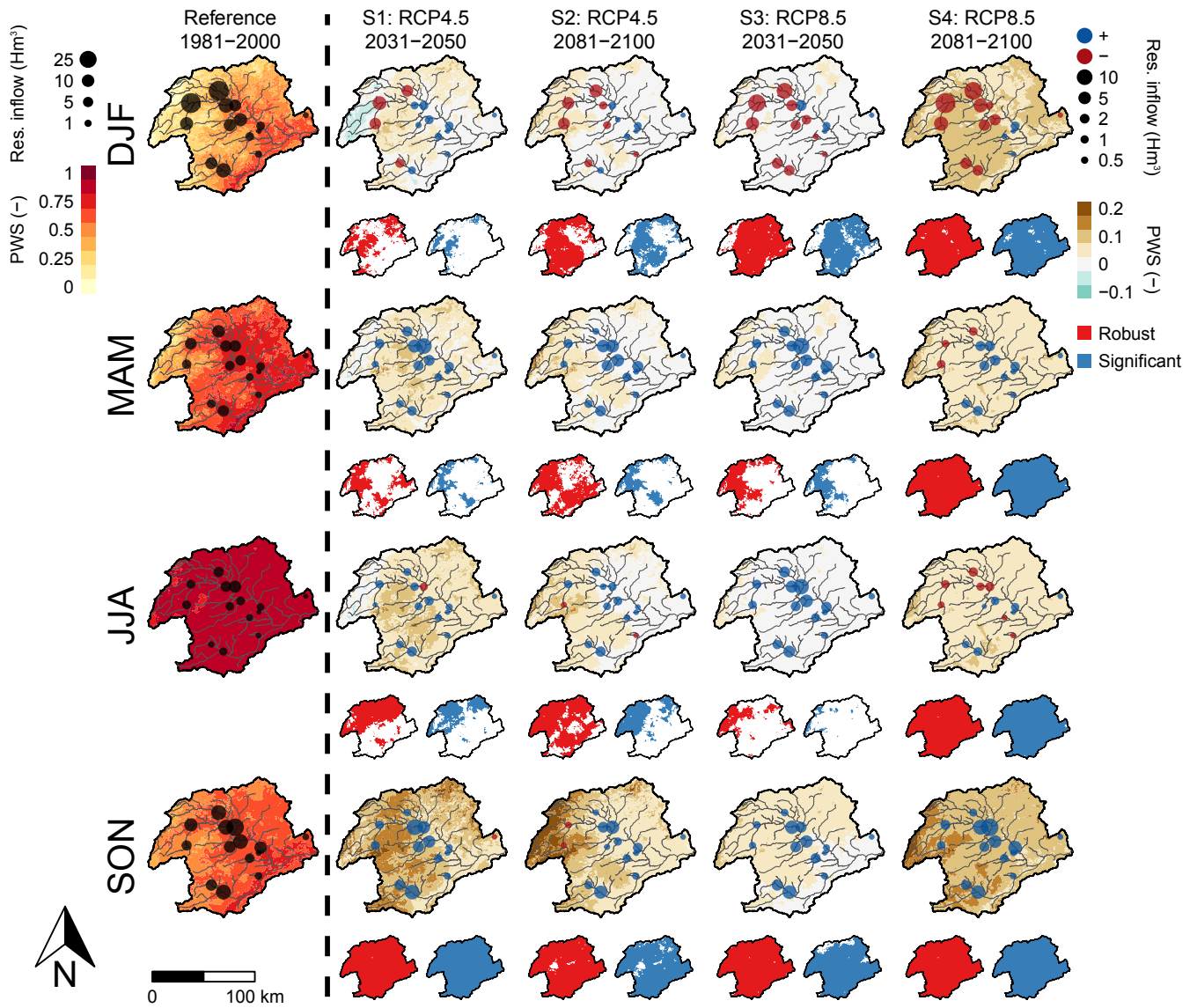
Figure 4. Ensemble average seasonal reservoir inflow (dots, Hm^3) and plant water stress (PWS) (-) for the reference scenario (left) and changes between the reference scenario and the four future scenarios (right), differentiated by season: winter (DJF), spring (MAM), summer (JJA), and autumn (SON). For the future scenarios, the reservoir inflow is presented as an increase (blue) or a decrease (red).

The increase in catchment-average hillslope erosion ranges from 24% (p=0.13) to 46% (p=0.01). Reservoir sediment yield increases in scenarios S1-3 and decreases in scenario S4. However, significant changes in sediment yield are only observed in scenario S4, with a decrease of 33% (p<0.01) due to decreasing sediment transport capacity in channels.
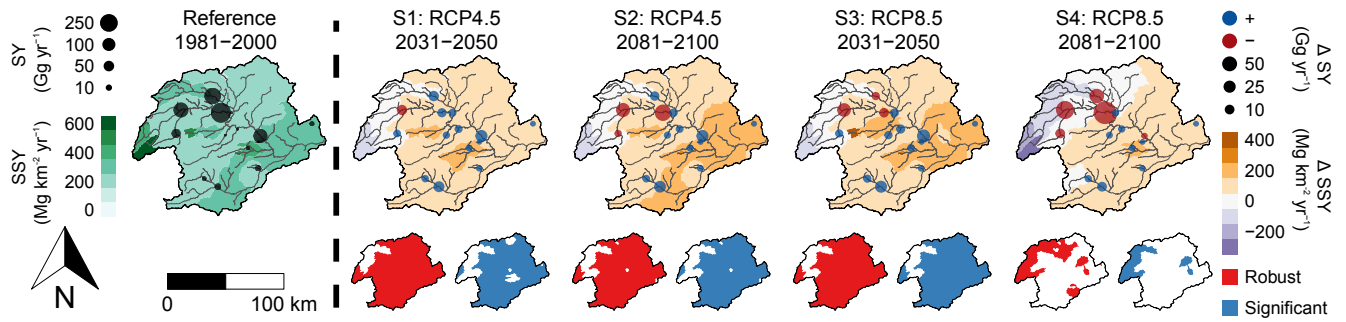
Figure 5. Ensemble average sediment yield (SY) at the reservoirs (dots, $\mathrm{Gg\,yr^{-1}}$) and average hillslope erosion (SSY) per subcatchment ($\mathrm{Mg\,km^{-2}\,yr^{-1}}$) for the reference scenario (left) and changes between the reference scenario and the four future scenarios (right). For the future scenarios, the SY is presented as an increase (blue) or a decrease (red).

4 Discussion and Conclusions

Previous studies concluded that climate change leads to reduced water availability in those areas where lower future annual precipitation sums are projected, evidenced by increased drought indices and reduced streamflow (Sperna Weiland et al., 2012; Arnell and Gosling, 2013; Lopez-Bustins et al., 2013; Forzieri et al., 2014). Our results confirm this, but more importantly we show a significant redistribution of water under future climate conditions, resulting in increased plant water stress due to a reduction of soil water content (green water), increased soil erosion and water inflow into streams and reservoirs (blue water), leading to an overall reduced water security. The redistribution of water is mainly driven by an increase in extreme precipitation and a decrease of precipitation frequency, and to a lesser extent by a change in annual precipitation volume (Fig. 2 and S4). The increase in extreme precipitation causes an increase in surface runoff and, subsequently, an increase in reservoir inflow and soil erosion. As such, climate change eventually leads to a reduction of infiltration into the soil, which negatively affects soil moisture content (Table S5) and, subsequently, leads to an increase in plant water stress (Fig. 4 and Table S4), which is a crucial impact indicator for agriculture and natural ecosystems, and may point towards reduced crop yield and natural vegetation cover (Allen et al., 1998).

The four climate change scenarios can be subdivided into moderate (scenarios S1-3) and extreme (scenario S4) climate conditions and related impacts. The moderate climate conditions are mainly characterized by limited reductions of annual precipitation sum and increased temperature (Fig. 3). This results in increase of plant water stress, due to a decrease of (actual) evapotranspiration and soil moisture content (Table S5). The extreme climate conditions (scenario S4) are characterized by a significant decrease of precipitation and an increase of dry spells and average temperature (Fig. 3). An increase of temperature often leads to an increase of evapotranspiration, however, less water will infiltrate into the soil due to the significant decrease of precipitation and its increased intensity. As a result, actual evapotranspiration and soil moisture content significantly decrease under these extreme conditions (Table S5), leading to a significant increase of plant water stress in all seasons (Fig. 4).

Previous studies indicated that soil erosion can either decrease or increase under climate change due to the combined effect of decreasing precipitation, increasing intensity and changing vegetation cover (Li and Fang, 2016). Our results show an increase in hillslope erosion due to increased precipitation intensity in the majority of the subcatchments, leading to an increase of sediment yield in most reservoirs (Fig. 5). Increased soil erosion may affect water security directly due to its effect on soil depth,

5   loss of soil organic matter content, and reduced water retention capacity. However, despite the increased soil erosion rates, the catchment-total reservoir sediment yield remains constant or even decreases, due to a decrease in the transport capacity of the flow resulting from a decrease in runoff in the headwaters, most pronounced in scenario S4. This further illustrates the importance of accounting for sediment transport capacity and the different response of hillslope erosion as compared to catchment sediment yield, which is still insufficiently accounted for in the current model and one of the main challenges in

10   soil erosion and sediment yield models (de Vente et al., 2013). So, although we did not find significantly increased reservoir storage capacity loss due to climate change in our study, loss of reservoir storage capacity is an important aspect affecting water security in many areas worldwide and requires attention when assessing water security (de Vente et al., 2005; Wisser et al., 2013).

Increased precipitation intensity leads to increased surface runoff, soil erosion, and redistribution of water within the catch-

15   ment. It is well established that extreme precipitation leads to surface runoff (Beven, 2012) and significantly contributes to soil erosion (Favis-Mortlock and Mullan, 2011), however, most large-scale impact assessments do not consider the most relevant process involved, i.e. infiltration excess surface runoff. A rough preliminary estimate indicates infiltration excess surface runoff actually plays a substantial role in about one quarter of the global land surface (Fig. 6), where extreme precipitation intensity exceeds the infiltration capacity of the soil. Therefore, we argue that, to account for the impact of increased extreme precipi-

20   tation on water security, it is crucial to consider infiltration excess surface runoff in hydrological and soil erosion assessments. Here, we introduced a new infiltration excess surface runoff equation (Eq. S1-S3), which runs at a daily ~~timestep~~ time step and meets the constraints of the available daily climate model output. The equation requires sub-daily precipitation data as input, i.e. the fraction of daily rainfall that occurs in the hour with the highest intensity, which we obtained from local hourly precipitation timeseries. While we show that extreme precipitation may increase under future climate change, the sub-daily

25   precipitation distribution may change as well. Hence, the impact of extreme precipitation on water security may only be fully assessed when climate models also provide sub-daily precipitation data. Furthermore, we applied a bias-correction method (quantile mapping) that explicitly accounts for changes in the projected daily precipitation distribution. Many previous studies applied the change factor (or delta change) method, which does not fully account for the changes in rainfall intensity. Studies that apply this method often show that a change of annual rainfall leads to a similar direction of change of runoff and soil

30   erosion (e.g., Shrestha et al., 2013; Correa et al., 2016). Therefore, future studies should consider bias-correction methods that account for changes in frequency and intensity of extreme events that affect both hydrology and soil erosion (Mullan et al., 2012; Li and Fang, 2016).

Our analysis further shows that, in general, plant water stress and reservoir inflow both increase under future climate conditions. For agriculture, which amounts to more than 40% of the catchment surface area, this may have significant consequences.

35   Rainfed crops (covering 31% of the catchment) are most affected by increases in plant water stress (Fig. S7). Seasonal changes
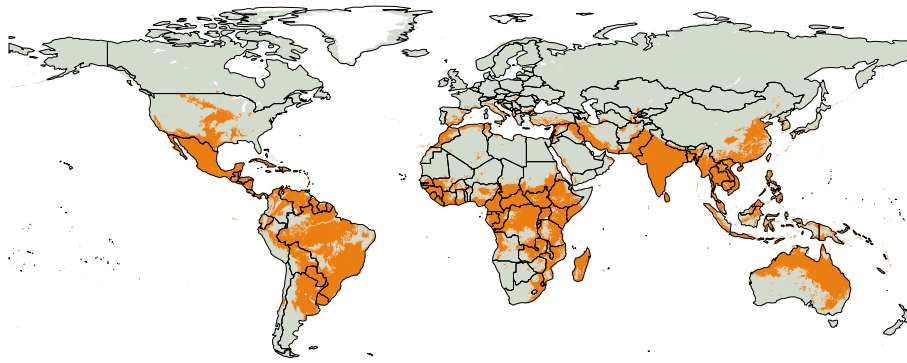
Figure 6. Global map indicating the areas (in orange) prone for infiltration excess surface runoff, defined as those areas where extreme precipitation exceeds the infiltration rate (Figure S2). See SI for more details.

in plant water stress (i.e. increase plant water stress in autumn), will strongly affect the harvest and seeding period of the dominant rainfed crops (e.g. (winter) cereal and almonds), which may lead to decreasing crop yields (Allen et al., 1998). On the other hand, increased reservoir inflow may be beneficial for irrigated agriculture (covering 12% of the catchment). The current annual irrigated water demand equals 1101 Hm^3 (Confederación Hidrolgráfica del Segura, 2015). Hence, 36-46% of

5 the irrigated water demand can be met with the annual natural reservoir inflow under future climate conditions. However, an increase of plant water stress is also projected for irrigated crops (Fig. S7), which would lead to increasing water demand. In this study we did not account for additional water supply from deep aquifers and the Tagus-Segura water transfer, neither for the supply of water to irrigated agriculture. In this way, our results deliberately emphasize the changes in water availability that result from climate change and from changes in water demand from natural ecosystems and rainfed agriculture. Currently,

10 irrigation water demand is partly met with water abstractions from deep aquifers and from the Tagus-Segura water transfer. Previous studies have shown that the deep aquifers in the study area are already overexploited (Rupérez-Moreno et al., 2017; Pellicer-Martínez and Martínez-Paz, 2018), which reduces the prospects for future irrigation water extraction. Furthermore, the already highly debated Tagus-Segura water transfer will most likely suffer from reduced water supply under future climate conditions (Lobanova et al., 2017). While increasing water supply from reservoirs is projected, the future sustainability of

15 irrigated crops will most likely decrease due to increased plant water stress, depleted aquifers and reduced water supply from the Tagus-Segura water transfer.

These changes also have other long-term consequences. Increasing plant water stress in rainfed agriculture may cause a shift from rainfed to irrigated agriculture, a trend that is already taking place (Nainggolan et al., 2012) and that would increase the dependency on reservoir storage and irrigation infrastructure. Further land abandonment can be foreseen in areas without access

20 to irrigation water, leading to an increase of shrubland and forest, with significant consequences for ecosystem functioning and rural livelihoods and possible decreased streamflow (Beguería et al., 2003; García-Ruiz et al., 2011). On the other hand, our findings illustrate that careful design of land management in rainfed areas can directly affect water availability for irrigated

agriculture, i.e. water available in reservoirs. The design of climate change adaptation strategies should therefore consider their effect on the redistribution of water from green to blue water and the long-term socio-economic consequences. For example, sustainable land management can possibly form a more cost-effective adaptation option to increased extreme precipitation than investing in larger reservoirs and irrigation infrastructure (Sanz et al., 2017).

5   Overall, our results illustrate that representation of pertinent hydrological processes and suitable bias-correction methods are crucial for accurate climate change impact assessments. To increase water security under climate change we show there is a need for effective adaptation strategies that aim to increase the water holding capacity of the soil (green water) and to reduce soil erosion in order to enhance soil quality and maintain the storage capacity of reservoirs (blue water), benefiting rainfed and irrigated agriculture.

References

Allen, R. G., Pereira, L., Raes, D., and Smith, M.: Crop evapotranspiration: Guidelines for computing crop requirements, Tech. Rep. 56, FAO, https://doi.org/10.1016/j.eja.2010.12.001, http://www.kimberly.uidaho.edu/water/fao56/fao56.pdf, 1998.

Arnell, N. W. and Gosling, S. N.: The impacts of climate change on river flow regimes at the global scale, Journal of Hydrology, 486, 351–364, https://doi.org/10.1016/j.jhydrol.2013.02.010, http://dx.doi.org/10.1016/j.jhydrol.2013.02.010http://linkinghub.elsevier.com/retrieve/pii/S0022169413001224, 2013.

Baartman, J. E. M., Jetten, V. G., Ritsema, C. J., and de Vente, J.: Exploring effects of rainfall intensity and duration on soil erosion at the catchment scale using openLISEM: Prado catchment, SE Spain, Hydrological Processes, 26, 1034–1049, https://doi.org/10.1002/hyp.8196, http://doi.wiley.com/10.1002/hyp.8196, 2012.

Beguería, S., López-Moreno, J. I., Lorente, A., Seeger, M., and García-Ruiz, J. M.: Assessing the effect of climate oscillations and land-use changes on streamflow in the central Spanish Pyrenees., Ambio, 32, 283–6, http://www.ncbi.nlm.nih.gov/pubmed/12956594, 2003.

Beven, K. J.: Rainfall-runoff modelling: the primer, John Wiley & Sons, Ltd, Chichester, UK, https://doi.org/10.1002/9781119951001, http://www.scopus.com/inward/record.url?eid=2-s2.0-84888749158{&}partnerID=tZOtx3y1, 2012.

Castillo, V. M., Gómez-Plaza, A., and Martínez-Mena, M.: The role of antecedent soil water content in the runoff response of semiarid catchments: A simulation approach, Journal of Hydrology, 284, 114–130, https://doi.org/10.1016/S0022-1694(03)00264-6, 2003.

Confederación Hidrolgráfica del Segura: Plan Hidrológico de la Cuenca del Segura. 2015-2021., Tech. rep., Confederación Hidrolgráfica del Segura, Murcia, Spain, 2015.

Correa, S. W., Mello, C. R., Chou, S. C., Curi, N., and Norton, L. D.: Soil erosion risk associated with climate change at Mantaro River basin, Peruvian Andes, CATENA, 147, 110–124, https://doi.org/10.1016/j.catena.2016.07.003, http://dx.doi.org/10.1016/j.catena.2016.07.003http://linkinghub.elsevier.com/retrieve/pii/S0341816216302624, 2016.

de Vente, J., Poesen, J., and Verstraeten, G.: The application of semi-quantitative methods and reservoir sedimentation rates for the prediction of basin sediment yield in Spain, Journal of Hydrology, 305, 63–86, https://doi.org/10.1016/j.jhydrol.2004.08.030, http://linkinghub.elsevier.com/retrieve/pii/S0022169404004081, 2005.

de Vente, J., Poesen, J., Verstraeten, G., Govers, G., Vanmaercke, M., Van Rompaey, A., Arabkhedri, M., and Boix-Fayos, C.: Predicting soil erosion and sediment yield at regional scales: Where do we stand?, Earth-Science Reviews, 127, 16–29, https://doi.org/10.1016/j.earscirev.2013.08.014, http://dx.doi.org/10.1016/j.earscirev.2013.08.014http://www.scopus.com/inward/record.url?eid=2-s2.0-84885151270{&}partnerID=40{&}md5=9e85be75eb96248be9fa1e91d2f0ae13http://linkinghub.elsevier.com/retrieve/pii/S0012825213001475, 2013.

Donnelly, C., Greuell, W., Andersson, J., Gerten, D., Pisacane, G., Roudier, P., and Ludwig, F.: Impacts of climate change on European hydrology at 1.5, 2 and 3 degrees mean global warming above preindustrial level, Climatic Change, 143, 13–26, https://doi.org/10.1007/s10584-017-1971-7, http://link.springer.com/10.1007/s10584-017-1971-7, 2017.

Eekhout, J. P. C., Terink, W., and de Vente, J.: Assessing the large-scale impacts of environmental change using a coupled hydrology and soil erosion model, Earth Surface Dynamics, 6, 687–703, https://doi.org/10.5194/esurf-6-687-2018, https://www.earth-surf-dynam.net/6/687/2018/, 2018.

Farr, T. G., Rosen, P. A., Caro, E., Crippen, R., Duren, R., Hensley, S., Kobrick, M., Paller, M., Rodriguez, E., Roth, L., Seal, D., Shaffer, S., Shimada, J., Umland, J., Werner, M., Oskin, M., Burbank, D., and Alsdorf, D.: The Shuttle Radar Topography Mission, Reviews of Geophysics, 45, RG2004, https://doi.org/10.1029/2005RG000183, http://doi.wiley.com/10.1029/2005RG000183, 2007.

Favis-Mortlock, D. and Mullan, D.: Soil erosion by water under future climate change, in: Soil hydrology, land use and agriculture: measurement and modelling, edited by Shukla, M. K., pp. 384–414, CABI, Wallingford, UK, https://doi.org/10.1079/9781845937973.0384, http://www.cabi.org/cabebooks/ebook/20113256961, 2011.

Fay, P. A., Carlisle, J. D., Knapp, A. K., Blair, J. M., and Collins, S. L.: Productivity responses to altered rainfall patterns in a C 4 -dominated grassland, Oecologia, 137, 245–251, https://doi.org/10.1007/s00442-003-1331-3, http://link.springer.com/10.1007/s00442-003-1331-3, 2003.

Forzieri, G., Feyen, L., Rojas, R., Flörke, M., Wimmer, F., and Bianchi, A.: Ensemble projections of future streamflow droughts in Europe, Hydrology and Earth System Sciences, 18, 85–108, https://doi.org/10.5194/hess-18-85-2014, http://www.hydrol-earth-syst-sci.net/18/85/2014/, 2014.

García-Ruiz, J. M., López-Moreno, J. I., Vicente-Serrano, S. M., Lasanta–Martínez, T., and Beguería, S.: Mediterranean water resources in a global change scenario, Earth-Science Reviews, 105, 121–139, https://doi.org/10.1016/j.earscirev.2011.01.006, http://linkinghub.elsevier.com/retrieve/pii/S0012825211000134, 2011.

García-Ruiz, J. M., Nadal-Romero, E., Lana-Renault, N., and Beguería, S.: Erosion in Mediterranean landscapes: Changes and future challenges, Geomorphology, 198, 20–36, https://doi.org/10.1016/j.geomorph.2013.05.023, http://dx.doi.org/10.1016/j.geomorph.2013.05.023, 2013.

Heber Green, W. and Ampt, G. A.: Studies on Soil Phyics., The Journal of Agricultural Science, 4, 1–24, https://doi.org/10.1017/S0021859600001441, http://www.journals.cambridge.org/abstract{_}S0021859600001441, 1911.

Hengl, T., Mendes de Jesus, J., Heuvelink, G. B. M., Ruiperez Gonzalez, M., Kilibarda, M., Blagotić, A., Shangguan, W., Wright, M. N., Geng, X., Bauer-Marschallinger, B., Guevara, M. A., Vargas, R., MacMillan, R. A., Batjes, N. H., Leenaars, J. G. B., Ribeiro, E., Wheeler, I., Mantel, S., and Kempen, B.: SoilGrids250m: Global gridded soil information based on machine learning, PLOS ONE, 12, e0169 748, https://doi.org/10.1371/journal.pone.0169748, http://dx.plos.org/10.1371/journal.pone.0169748https://dx.plos.org/10.1371/journal.pone.0169748, 2017.

Herrera, S., Fernández, J., and Gutiérrez, J. M.: Update of the Spain02 gridded observational dataset for EURO-CORDEX evaluation: assessing the effect of the interpolation methodology, International Journal of Climatology, 36, 900–908, https://doi.org/10.1002/joc.4391, http://doi.wiley.com/10.1002/joc.4391, 2016.

Ivancic, T. J. and Shaw, S. B.: Examining why trends in very heavy precipitation should not be mistaken for trends in very high river discharge, Climatic Change, 133, 681–693, https://doi.org/10.1007/s10584-015-1476-1, http://link.springer.com/10.1007/s10584-015-1476-1, 2015.

Jacob, D., Petersen, J., Eggert, B., Alias, A., Christensen, O. B., Bouwer, L. M., Braun, A., Colette, A., Déqué, M., Georgievski, G., Georgopoulou, E., Gobiet, A., Menut, L., Nikulin, G., Haensler, A., Hempelmann, N., Jones, C., Keuler, K., Kovats, S., Kröner, N., Kotlarski, S., Kriegsmann, A., Martin, E., van Meijgaard, E., Moseley, C., Pfeifer, S., Preuschmann, S., Radermacher, C., Radtke, K., Rechid, D., Rounsevell, M., Samuelsson, P., Somot, S., Soussana, J.-F., Teichmann, C., Valentini, R., Vautard, R., Weber, B., and Yiou, P.: EURO-CORDEX: new high-resolution climate change projections for European impact research, Regional Environmental Change, 14, 563–578, https://doi.org/10.1007/s10113-013-0499-2, http://link.springer.com/10.1007/s10113-013-0499-2http://download.springer.com/static/pdf/221/art:10.1007/s10113-013-0499-2.pdf?originUrl=http://link.springer.com/article/10.1007/s10113-013-0499-2{&}token2=exp=1462793760{~}acl=/static/pdf/221/art:10.1007/s10, 2014.

Knapp, A. K., Beier, C., Briske, D. D., Classen, A. T., Luo, Y., Reichstein, M., Smith, M. D., Smith, S. D., Bell, J. E., Fay, P. A., Heisler, J. L., Leavitt, S. W., Sherry, R., Smith, B., and Weng, E.: Consequences of More Extreme Precipitation Regimes for Terrestrial

Ecosystems, BioScience, 58, 811–821, https://doi.org/10.1641/B580908, http://academic.oup.com/bioscience/article/58/9/811/250853/Consequences-of-More-Extreme-Precipitation-Regimes, 2008.

León-Sánchez, L., Nicolás, E., Goberna, M., Prieto, I., Maestre, F. T., and Querejeta, J. I.: Poor plant performance under simulated climate change is linked to mycorrhizal responses in a semi-arid shrubland, Journal of Ecology, 106, 960–976, https://doi.org/10.1111/1365-2745.12888, http://doi.wiley.com/10.1111/1365-2745.12888, 2018.

5 Lesschen, J., Schoorl, J., and Cammeraat, L.: Modelling runoff and erosion for a semi-arid catchment using a multi-scale approach based on hydrological connectivity, Geomorphology, 109, 174–183, https://doi.org/10.1016/j.geomorph.2009.02.030, http://dx.doi.org/10.1016/j.geomorph.2009.02.030http://linkinghub.elsevier.com/retrieve/pii/S0169555X09001007, 2009.

Li, Z. and Fang, H.: Impacts of climate change on water erosion: A review, Earth-Science Reviews, 163, 94–117, https://doi.org/10.1016/j.earscirev.2016.10.004, http://linkinghub.elsevier.com/retrieve/pii/S0012825216303555, 2016.

10 Lobanova, A., Liersch, S., Tàbara, J. D., Koch, H., Hattermann, F. F., and Krysanova, V.: Harmonizing human-hydrological system under climate change: A scenario-based approach for the case of the headwaters of the Tagus River, Journal of Hydrology, 548, 436–447, https://doi.org/10.1016/j.jhydrol.2017.03.015, http://dx.doi.org/10.1016/j.jhydrol.2017.03.015https://linkinghub.elsevier.com/retrieve/pii/S002216941730152X, 2017.

15 Lopez-Bustins, J. A., Pascual, D., Pla, E., and Retana, J.: Future variability of droughts in three Mediterranean catchments, Natural Hazards, 69, 1405–1421, https://doi.org/10.1007/s11069-013-0754-3, 2013.

Manus, C., Anquetin, S., Braud, I., Vandervaere, J.-P., Creutin, J.-D., Viallet, P., and Gaume, E.: A modelling approach to assess the hydrological response of small Mediterranean catchments to the variability of soil characteristics in a context of extreme events, Hydrology and Earth System Sciences Discussions, 5, 2687–2725, https://doi.org/10.5194/hessd-5-2687-2008, http://www.hydrol-earth-syst-sci-discuss.net/5/2687/2008/, 2008.

20 MAPAMA: Mapa de Cultivos y Aprovechamientos de España 2000-2010 (1: 50.000), http://www.magrama.gob.es/es/cartografia-y-sig/publicaciones/agricultura/mac{_}2000{_}2009.aspx, 2010.

Maraun, D., Shepherd, T. G., Widmann, M., Zappa, G., Walton, D., Gutiérrez, J. M., Hagemann, S., Richter, I., Soares, P. M. M., Hall, A., and Mearns, L. O.: Towards process-informed bias correction of climate change simulations, Nature Climate Change, 7, 664–773, https://doi.org/10.1038/nclimate3418, http://www.nature.com/doifinder/10.1038/nclimate3418, 2017.

25 Merheb, M., Moussa, R., Abdallah, C., Colin, F., Perrin, C., and Baghdadi, N.: Hydrological response characteristics of Mediterranean catchments at different time scales: a meta-analysis, Hydrological Sciences Journal, 61, 1–20, https://doi.org/10.1080/02626667.2016.1140174, http://www.tandfonline.com/doi/full/10.1080/02626667.2016.1140174, 2016.

Mishra, V., Dominguez, F., and Lettenmaier, D. P.: Urban precipitation extremes: How reliable are regional climate models?, Geophysical Research Letters, 39, n/a–n/a, https://doi.org/10.1029/2011GL050658, http://doi.wiley.com/10.1029/2011GL050658, 2012.

30 Morgan, R. P. C. and Duzant, J. H.: Modified MMF (Morgan–Morgan–Finney) model for evaluating effects of crops and vegetation cover on soil erosion, Earth Surface Processes and Landforms, 33, 90–106, https://doi.org/10.1002/esp.1530, http://doi.wiley.com/10.1002/esp.1530, 2008.

Mullan, D., Favis-Mortlock, D., and Fealy, R.: Addressing key limitations associated with modelling soil erosion under the impacts of future climate change, Agricultural and Forest Meteorology, 156, 18–30, https://doi.org/10.1016/j.agrformet.2011.12.004, http://dx.doi.org/10.1016/j.agrformet.2011.12.004, 2012.

Nainggolan, D., de Vente, J., Boix-Fayos, C., Termansen, M., Hubacek, K., and Reed, M. S.: Afforestation, agricultural abandonment and intensification: Competing trajectories in semi-arid Mediterranean agro-ecosystems, Agriculture, Ecosystems and Environment, 159, 90–104, https://doi.org/10.1016/j.agee.2012.06.023, http://dx.doi.org/10.1016/j.agee.2012.06.023, 2012.

Nearing, M., Deer-Ascough, L., and Laflen, J. M.: SENSITIVITY ANALYSIS OF THE WEPP HILLSLOPE PROFILE EROSION MODEL, Transactions of the ASAE, 33, 0839–0849, https://doi.org/10.13031/2013.31409, http://elibrary.asabe.org/abstract.asp??JID=3{&}AID= 31409{&}CID=t1990{&}v=33{&}i=3{&}T=1, 1990.

Nearing, M. A., Pruski, F. F., and O'Neal, M. R.: Expected climate change impacts on soil erosion rates: A review, Journal of Soil and Water Conservation, 59, 43–50, http://www.jswconline.org/content/59/1/43.abstract, 2004.

Nicholson, E., Mace, G. M., Armsworth, P. R., Atkinson, G., Buckle, S., Clements, T., Ewers, R. M., Fa, J. E., Gardner, T. A., Gibbons, J., Grenyer, R., Metcalfe, R., Mourato, S., Muûls, M., Osborn, D., Reuman, D. C., Watson, C., and Milner-Gulland, E. J.: Priority research areas for ecosystem services in a changing world, Journal of Applied Ecology, 46, 1139–1144, https://doi.org/10.1111/j.1365-2664.2009.01716.x, http://doi.wiley.com/10.1111/j.1365-2664.2009.01716.x, 2009.

Nunes, J. P., Seixas, J., and Pacheco, N. R.: Vulnerability of water resources, vegetation productivity and soil erosion to climate change in Mediterranean watersheds, Hydrological Processes, 22, 3115–3134, https://doi.org/10.1002/hyp.6897, http://jamsb.austms.org.au/courses/ CSC2408/semester3/resources/ldp/abs-guide.pdfhttp://doi.wiley.com/10.1002/hyp.6897, 2008.

Nunes, J. P., Seixas, J., Keizer, J. J., and Ferreira, A. J. D.: Sensitivity of runoff and soil erosion to climate change in two Mediterranean watersheds. Part I: model parameterization and evaluation, Hydrological Processes, 23, 1202–1211, https://doi.org/10.1002/hyp.7247, http://doi.wiley.com/10.1002/hyp.7247, 2009a.

Nunes, J. P., Seixas, J., Keizer, J. J., and Ferreira, A. J. D.: Sensitivity of runoff and soil erosion to climate change in two Mediterranean watersheds. Part II: assessing impacts from changes in storm rainfall, soil moisture and vegetation cover, Hydrological Processes, 23, 1212–1220, https://doi.org/10.1002/hyp.7250, http://doi.wiley.com/10.1002/hyp.7250, 2009b.

Nunes, J. P., Seixas, J., and Keizer, J. J.: Modeling the response of within-storm runoff and erosion dynamics to climate change in two Mediterranean watersheds: A multi-model, multi-scale approach to scenario design and analysis, Catena, 102, 27–39, https://doi.org/10.1016/j.catena.2011.04.001, 2013.

O'Gorman, P. a. and Schneider, T.: The physical basis for increases in precipitation extremes in simulations of 21st-century climate change., Proceedings of the National Academy of Sciences of the United States of America, 106, 14 773–14 777, https://doi.org/10.1073/pnas.0907610106, 2009.

Paroissien, J.-B., Darboux, F., Couturier, A., Devillers, B., Mouillot, F., Raclot, D., and Le Bissonnais, Y.: A method for modeling the effects of climate and land use changes on erosion and sustainability of soil in a Mediterranean watershed (Languedoc, France), Journal of Environmental Management, 150, 57–68, https://doi.org/10.1016/j.jenvman.2014.10.034, http://linkinghub.elsevier.com/retrieve/ pii/S030147971400526X, 2015.

Pellicer-Martínez, F. and Martínez-Paz, J. M.: Probabilistic evaluation of the water footprint of a river basin: Accounting method and case study in the Segura River Basin, Spain, Science of The Total Environment, 627, 28–38, https://doi.org/10.1016/j.scitotenv.2018.01.223, https://doi.org/10.1016/j.scitotenv.2018.01.223http://linkinghub.elsevier.com/retrieve/pii/S004896971830264X, 2018.

Pimentel, D., Harvey, C., Resosudarmo, P., Sinclair, K., Kurz, D., McNair, M., Crist, S., Shpritz, L., Fitton, L., Saffouri, R., and Blair, R.: Environmental and Economic Costs of Soil Erosion and Conservation Benefits, Science, 267, 1117–1123, https://doi.org/10.1126/science.267.5201.1117, http://www.sciencemag.org/cgi/doi/10.1126/science.267.5201.1117, 1995.

Porporato, A., Laio, F., Ridolfi, L., and Rodriguez-Iturbe, I.: Plants in water-controlled ecosystems: active role in hydrologic processes and response to water stress, Advances in Water Resources, 24, 725–744, https://doi.org/10.1016/S0309-1708(01)00006-9, http://linkinghub.elsevier.com/retrieve/pii/S0309170801000070http://linkinghub.elsevier.com/retrieve/pii/S0309170801000069, 2001.

Pruski, F. F. and Nearing, M. A.: Runoff and soil loss responses to changes in precipitation: A computer simulation study, Journal of Soil and Water Conservation, 57, 7–16, 2002.

Routschek, A., Schmidt, J., and Kreienkamp, F.: Impact of climate change on soil erosion - A high-resolution projection on catchment scale until 2100 in Saxony/Germany, Catena, 121, 99–109, https://doi.org/10.1016/j.catena.2014.04.019, http://dx.doi.org/10.1016/j.catena.2014.04.019, 2014.

Rupérez-Moreno, C., Senent-Aparicio, J., Martinez-Vicente, D., García-Aróstegui, J. L., Calvo-Rubio, F. C., and Pérez-Sánchez, J.: Sustainability of irrigated agriculture with overexploited aquifers: The case of Segura basin (SE, Spain), Agricultural Water Management, 182, 67–76, https://doi.org/10.1016/j.agwat.2016.12.008, http://dx.doi.org/10.1016/j.agwat.2016.12.008http://linkinghub.elsevier.com/retrieve/pii/S0378377416304978, 2017.

Sanz, M. J., de Vente, J., Chotte, J. L., Bernoux, M., Kust, G., Ruiz, I., Almagro, M., Alloza, J. A., Vallejo, R., Castillo, V., Hebel, A., and Akhtar-Schuster, M.: Sustainable Land Management contribution to successful land-based climate change adaptation and mitigation. A Report of the Science-Policy Interface. United Nations Convention to Combat Desertification (UNCCD), Tech. rep., UNCCD SPI, Bonn, Germany, 2017.

Serrano-Notivoli, R., Beguería, S., Saz, M. Á., Longares, L. A., and de Luis, M.: SPREAD: a high-resolution daily gridded precipitation dataset for Spain – an extreme events frequency and intensity overview, Earth System Science Data, 9, 721–738, https://doi.org/10.5194/essd-9-721-2017, https://www.earth-syst-sci-data.net/9/721/2017/, 2017.

Shrestha, B., Babel, M. S., Maskey, S., van Griensven, A., Uhlenbrook, S., Green, A., and Akkharath, I.: Impact of climate change on sediment yield in the Mekong River basin: a case study of the Nam Ou basin, Lao PDR, Hydrology and Earth System Sciences, 17, 1–20, https://doi.org/10.5194/hess-17-1-2013, http://www.hydrol-earth-syst-sci.net/17/1/2013/, 2013.

Sillmann, J., Kharin, V. V., Zwiers, F. W., Zhang, X., and Bronaugh, D.: Climate extremes indices in the CMIP5 multimodel ensemble: Part 2. Future climate projections, Journal of Geophysical Research: Atmospheres, 118, 2473–2493, https://doi.org/10.1002/jgrd.50188, http://doi.wiley.com/10.1002/jgrd.50188, 2013.

Sperna Weiland, F. C., Van Beek, L. P. H., Kwadijk, J. C. J., and Bierkens, M. F. P.: Global patterns of change in discharge regimes for 2100, Hydrology and Earth System Sciences, 16, 1047–1062, https://doi.org/10.5194/hess-16-1047-2012, 2012.

Sun, Y., Solomon, S., Dai, A., and Portmann, R. W.: How often will it rain?, Journal of Climate, 20, 4801–4818, https://doi.org/10.1175/JCLI4263.1, 2007.

Terink, W., Lutz, A. F., Simons, G. W. H., Immerzeel, W. W., and Droogers, P.: SPHY v2.0: Spatial Processes in HYdrology, Geoscientific Model Development, 8, 2009–2034, https://doi.org/10.5194/gmd-8-2009-2015, http://www.geosci-model-dev.net/8/2009/2015/, 2015.

Themeßl, M. J., Gobiet, A., and Leuprecht, A.: Empirical-statistical downscaling and error correction of daily precipitation from regional climate models, International Journal of Climatology, 31, 1530–1544, https://doi.org/10.1002/joc.2168, http://doi.wiley.com/10.1002/joc.2168, 2011.

Themeßl, M. J., Gobiet, A., and Heinrich, G.: Empirical-statistical downscaling and error correction of regional climate models and its impact on the climate change signal, Climatic Change, 112, 449–468, https://doi.org/10.1007/s10584-011-0224-4, http://link.springer.com/10.1007/s10584-011-0224-4, 2012.

Thober, S., Kumar, R., Wanders, N., Marx, A., Pan, M., Rakovec, O., Samaniego, L., Sheffield, J., Wood, E. F., and Zink, M.: Multi-model ensemble projections of European river floods and high flows at 1.5, 2, and 3 degrees global warming, Environmental Research Letters, 13, 014 003, https://doi.org/10.1088/1748-9326/aa9e35, http://iopscience.iop.org/article/10.1088/1748-9326/aa9e35http://stacks.iop.org/1748-9326/13/i=1/a=014003?key=crossref.c93f4ad828d9152aa572057fa0c67675, 2018.

5 UN-Water: Water Security & the Global Water Agenda - A UN-Water Analytical Brief, United Nations University, 2013.

United Nations General Assembly: Transforming our world: The 2030 agenda for sustainable development, Tech. Rep. October, United Nations, http://unctad.org/meetings/en/SessionalDocuments/ares70d1{_}en.pdf, 2015.

Wasko, C. and Sharma, A.: Global assessment of flood and storm extremes with increased temperatures, Scientific Reports, 7, 7945, https://doi.org/10.1038/s41598-017-08481-1, http://www.nature.com/articles/s41598-017-08481-1, 2017.

10 Wisser, D., Frolking, S., Hagen, S., and Bierkens, M. F. P.: Beyond peak reservoir storage? A global estimate of declining water storage capacity in large reservoirs, Water Resources Research, 49, 5732–5739, https://doi.org/10.1002/wrcr.20452, http://doi.wiley.com/10.1002/wrcr.20452, 2013.

Zhang, Y., Hernandez, M., Anson, E., Nearing, M. A., Wei, H., Stone, J. J., and Heilman, P.: Modeling climate change effects on runoff and soil erosion in southeastern Arizona rangelands and implications for mitigation with conservation practices, Journal of Soil and Water
15 Conservation, 67, 390–405, https://doi.org/10.2489/jswc.67.5.390, http://dx.doi.org/10.2489/jswc.67.5.390, 2012.

1 Model Description

We applied the Spatial Processes in HYdrology (SPHY) hydrological model (Terink et al., 2015), which is a spatially distributed leaky-bucket type of model applied on a cell-by-cell basis at a daily time step. The SPHY model is fully coupled with the Morgan-Morgan-Finney soil erosion model (MMF; Morgan and Duzant, 2008). The SPHY-MMF model is described in detail in Eekhout et al. (2018) and can be accessed at this location: https://github.com/JorisEekhout/SPHY/tree/SPHY2.1-MMF.

1.1 Hydrological Model

SPHY simulates most relevant hydrological processes, such as interception, evapotranspiration, dynamic evolution of vegetation cover (including seasonal patterns and response to climate change), surface runoff, and lateral and vertical soil moisture flow. Here we describe the main modification we made for this study, i.e. the inclusion of a infiltration excess surface runoff equation. See Terink et al. (2015) for a detailed description of the model.

The previous version of the SPHY model only accounted for saturation excess surface runoff. Here, we also account for infiltration excess surface runoff, with a new infiltration excess surface runoff equation, which runs at a daily time step. The equation is inspired by the Green-Ampt ~~formula~~ equation (Heber Green and Ampt, 1911). We assumed a constant infiltration rate f ($\mathrm{mm\,hr^{-1}}$), which is determined for each cell and each day by:

$$f = \frac{K_{\text{eff}}}{24} \left[1 + \frac{\theta_{\text{sat}} - \theta}{\theta_{\text{sat}}}\right]^{\lambda} \tag{S1}$$

where K_{eff} is the effective hydraulic conductivity, θ_{sat} is the saturated water content, θ is the ~~actual water content~~ initial soil moisture content at time step t, and λ is a calibration parameter. Bouwer (1969) suggested an approximation of $K_{\text{eff}} \approx 0.5 K_{\text{sat}}$. Equation S1 deviates for some aspects from the original Green-Ampt equation. The soil moisture content θ is the soil moisture content of the previous time step. We divide by θ_{sat} to account for the differences in soil properties, which are originally expressed by the matric suction head at the wetting front. The cumulative infiltration in the Green-Ampt equation reduces the infiltration capacity in each subsequent time step. To account for this non-linear behaviour, we included the calibration parameter λ. This simplification of the Green-Ampt equation is considered justified for assessments with a daily time step and for large study areas with a coarse spatial resolution.

Infiltration excess surface runoff occurs when the precipitation intensity exceeds the infiltration rate f (Beven, 2012). Analysis of hourly precipitation time series for 25 years (1991-2015) from 5 precipitation stations in the catchment showed that, on average, the highest precipitation intensity was recorded in the first hour of the rain storm and decreases linearly until the end of the storm. We assumed a triangular-shaped precipitation intensity $p(t)$ ($\mathrm{mm\,hr^{-1}}$) according to:

$$p(t) = -\frac{1}{2}\alpha^2 P t + \alpha P \tag{S2}$$

where α is the fraction of daily rainfall that occurs in the hour with the highest intensity, P is the daily rainfall (mm), and t is an hourly time step. Daily infiltration excess surface runoff Q_{surf} is determined as follows:

$$Q_{\text{surf}} = \begin{cases} \dfrac{(\alpha P - f)^2}{\alpha^2 P} & \text{if } \alpha P > f \\ 0 & \text{if } \alpha P \leq f \end{cases} \tag{S3}$$

When the hourly precipitation intensity αP is higher than the infiltration rate f, surface runoff equals the triangular shaped area of the precipitation above the infiltration rate. The amount of precipitation below the infiltration rate will infiltrate into the rootzone. Parameter α was set to 0.34, which follows from the analysis of the hourly rainfall data.

1.2 Daily Morgan-Morgan-Finney soil erosion model

We integrated the Morgan-Morgan-Finney (MMF; Morgan and Duzant, 2008) soil erosion model into the SPHY hydrological model. MMF is a conceptual soil erosion model that originally is applied at an annual time step. We modified the original

MMF model such that it runs at a daily time step and is fully integrated into the SPHY model. This means that MMF receives input from the SPHY model, such as effective precipitation (throughfall), runoff and canopy cover.

Detachment of soil particles is determined separately for raindrop impact and surface runoff. The detachment of soil particles by raindrop impact (F; kg m^{-2}) is a function of the kinetic energy of the effective rainfall, the detachability of the soil (K; J m^{-2}) and the ground cover (GC; expressed as a proportion between zero and unity). The kinetic energy of the effective rainfall is in turn determined separately for direct throughfall and leaf drainage, and is subsequently summed to obtain the total rainfall energy KE. Canopy cover (fraction between 0 and 1 and obtained from the dynamic vegetation module) is used to separate direct throughfall and leaf drop from effective precipitation. The ground cover protects the soil from detachment and includes the proportion of vegetation and stones covering the surface and is set to 1 in case of the presence of snow. In order to allow for the particle-size distribution of the soil, the effective rainfall is proportioned according to the proportion of clay (c), silt (z) and sand (s) particles in the soil and subsequently summed:

$$F_i = K_i \frac{\%i}{100}(1 - GC)KE \times 10^{-3} \tag{S4}$$

With i the textural class, i.e. c for clay, z for silt and s for sand. Based on data from Quansah (1982), values of K_c, K_z and K_s are taken respectively as 0.1, 0.5 and 0.3 g J^{-1}.

The detachment of soil particles by runoff (H; kg m^{-2}) is a function of the volume of accumulated runoff (Q; mm), the detachability of the soil by runoff (DR; g mm^{-1}), the slope angle (S; °) and the ground cover (GC; -). The detachment by runoff is also proportioned by texture class and subsequently summed:

$$H_i = DR_i \frac{\%i}{100}Q^{1.5}(1 - GC)\sin^{0.3} S \times 10^{-3} \tag{S5}$$

Based on data from Quansah (1982), values of DR_c, DR_z and DR_s are taken respectively as 1.0, 1.6 and 1.5 g mm^{-1}.

The detachment of soil particles by raindrop impact (F) and runoff (H) are subsequently summed. Only a proportion of the detached soil will be delivered to the runoff for transport, the remainder will be deposited within the cell of its origin. The percentage of the detached sediment that is deposited within the cell of its origin is estimated from the relationship obtained by Tollner et al. (1976), calculated separately for each particle size:

$$DEP_{c,z,s} = 44.1 N_{f_{c,z,s}}^{0.29} \tag{S6}$$

Where N_f is the particle fall number and DEP is maximized by 100. The particle fall number is a function of the flow velocity, which is a function of the presence and abundance of vegetation and the surface roughness.

The amount of soil particles that will be delivered to the runoff for transport is calculated as follows:

$$G = \sum_{c,z,s}(F_{c,z,s} + H_{c,z,s})(1 - (DEP_{c,z,s}/100)) \tag{S7}$$

1.3 Sediment Routing

Transport of sediment by runoff is restricted by the transport capacity of the flow. We modified the transport capacity equation as proposed by Prosser and Rustomji (2000) by introducing a landuse-specific roughness factor:

$$TC = \text{flow}_{\text{factor}}q^{\beta} S^{\gamma} \tag{S8}$$

Where $\text{flow}_{\text{factor}}$ is a spatially distributed roughness factor, q is the accumulated runoff per unit width ($\text{m}^2 \text{ day}^{-1}$), S is the local energy gradient, approximated by the slope, and β and γ are model parameters. As suggested by Prosser and Rustomji (2000) we set $\gamma = 1.4$ and we used β in the calibration procedure. The landuse-specific roughness factor $\text{flow}_{\text{factor}}$ is a function of the presence and abundance of vegetation and the surface roughness.

Reservoir sediment trapping efficiency, the percentage of sediment trapped by the reservoir, is calculated according to Brown (1943):

$$TE = 100\left[1 - \frac{1}{1 + 0.0021D\frac{C}{A_{\text{basin}}}}\right] \tag{S9}$$

where TE is the trapping efficiency (%), D is a constant within the range 0.046-1, we adopted the mean value of 0.1, C is the reservoir capacity (m^3), and A_{basin} is the drainage area of the subcatchment (km^2).

1.4 Dynamic Vegetation Module

SPHY-MMF includes a dynamic vegetation module that allows characterization of the seasonal and inter-annual differences in vegetation cover. A time series of the Normalized Difference Vegetation Index (NDVI) images is used as input for the dynamic vegetation module. The Leaf Area Index (LAI) is determined from the individual NDVI images using a logarithmic relation (Sellers et al., 1996). The LAI is used in the hydrological model to determine canopy storage, interception and the resulting precipitation throughfall. The latter is subsequently used in both the hydrological and soil erosion model. The canopy cover, from the soil erosion model, is defined as the LAI maximized by 1. The NDVI is also used to determine the crop coefficients, which are used in the calculation of the potential evapotranspiration. Crop coefficients are determined from NDVI with a linear relation. See Terink et al. (2015) for a detailed description of the dynamic vegetation module.

1.5 Model input data

All model input data were prepared at a 200 m resolution. Textural fractions (sand, clay and silt) and organic matter content were obtained from the global SoilGrids dataset (Hengl et al., 2017) at 250 m resolution. The soil hydraulic properties (saturated hydraulic conductivity, saturated water content, field capacity, and wilting point) were obtained by applying pedotransfer functions (Saxton and Rawls, 2006).

The SRTM dataset (Farr et al., 2007) at 30 m resolution was resampled to the model grid to obtain a Digital Elevation Model (Fig. 1d). The spatially distributed rock fraction map was obtained by applying the empirical formulations from Poesen et al. (1998), which determines rock fraction based on slope.

Both the hydrological and the soil erosion model require landuse-specific input. We used a national landuse map (MAPAMA, 2010), which provides 57 landuse classes within the study area. Values for the landuse-specific tabular value of the depletion fraction were obtained from Allen et al. (1998) (Table 22). Values for the maximum LAI were obtained from Sellers et al. (1996). The soil erosion model requires landuse-specific input for plant height, stem density, stem diameter, canopy cover fraction, ground cover fraction and Manning's roughness coefficient for vegetation. We obtained values for each of these parameters through observations from aerial photographs, expert judgement and as part of the calibration procedure.

NDVI images were obtained from bi-monthly Moderate Resolution Imaging Spectroradiometer (MODIS) data for the period 2000-2012. For model calibration (2001-2010) we used each of the individual NDVI images, after gap-filling (mainly due to cloud cover) with the long-term average 16-day period NDVI for the period 2000-2012.

For the reference and future scenarios no NDVI images of sufficient quality and resolution were available, therefore we prepared the NDVI model input, accounting for the intra- and inter-annual variability. The intra-annual variability was obtained from the long-term average 16-day period NDVI for the period 2000-2012. The inter-annual variability was determined based on a log-linear relationship between the annual precipitation sum, annual average temperature, annual maximum temperature and annual average NDVI for each of the 57 landuse classes for the period 2000-2012:

$$
\begin{aligned}
NDVI_{\text{year}} = {} & \beta_0 + \log(P_{\text{year}})\beta_1 + \log(P_{\text{year-1}})\beta_2 + \log(Tavg_{\text{year}})\beta_3 \\
& + \log(Tavg_{\text{year-1}})\beta_4 + \log(Tmax_{\text{year}})\beta_5 + \log(Tmax_{\text{year-1}})\beta_6
\end{aligned}
\tag{S10}
$$

Where $NDVI$ is the annual average NDVI, P the annual precipitation sum, $Tavg$ the annual average temperature, $Tmax$ the annual maximum temperature, and β_{0-6} coefficients of the log-linear regression model. We used the annual climate indices of two years, the current year and the previous year, to account for the climate lag that may influence the vegetation development. A stepwise model selection procedure was applied for each of the 57 landuse classes, selecting the best combination of variables from Eq. S10 with the lowest AIC (Akaike Information Criterion) in R (version 3.4.0), using the stepAIC algorithm from the MASS package (Venables and Ripley, 2002).

1.6 Model Calibration & Validation

Model calibration and validation were performed in five headwater subcatchments that are not affected by water extractions for irrigation (Fig. 1b). To prevent overfitting and achieve most realistic model calibration we set most of the potential calibration parameters at literature values and maintained the other parameters within reasonable physical limits of the parameter domain. Calibration and validation were performed for the periods 2001-2010 and 1987-2000, respectively. These periods were chosen such that we could make best use of the limited available data, i.e. daily discharge, precipitation, temperature and NDVI images.

Daily discharge time series were used to determine model performance. Data were obtained from the Segura River Basin Agency for the Fuensanta reservoir (Fig. 1b). We only considered the discharge originating from the Fuensanta subcatchment, by subtracting the discharge from the upstream located subcatchments, both for the observed and the simulated time series. The calibration procedure consisted of two steps. First, we optimized the water balance by comparing the observed and simulated discharge sum (percent bias). We adjusted the calibration parameter λ from Eq. S3 and model parameters from the dynamic vegetation module and soil hydraulic properties to optimize the percent bias of the discharge (Table S1). In the second step we optimized the Nash-Sutcliffe model efficiency (NSE; Nash and Sutcliffe, 1970) by adjusting a model parameter from the routing module (kx). The calibration resulted in a NSE of 0.47 for the daily discharge, a NSE of 0.76 for the monthly discharge and a percent bias of 2.3% (Fig. S1a). Model validation resulted in a NSE of 0.25 for the daily discharge, a NSE of 0.39 for the monthly discharge and a percent bias of -18.7% (Fig. S1b).

Next, we calibrated the soil erosion model. First, we optimized the detached material going into transport G for 8 aggregated landuse classes, based on literature data (Cerdan et al., 2010; Maetens et al., 2012), see Eekhout et al. (2018) (Table 1) for an overview of the model parameters per land use class. We optimized sediment yield at the reservoirs with reservoir sediment yield data from 4 reservoirs (Avendaño-Salas et al., 1997) (Fig. 1b). Model performance was evaluated based on percent bias. The calibration procedure focused on a model parameter from the sediment transport module. We obtained a percent bias of 0.0% in the calibration and -19.8% in the validation.

2 Global Infiltration Excess Surface Runoff

Infiltration excess surface runoff occurs when the precipitation intensity exceeds the soil infiltration rate (Beven, 2012). Based on global precipitation and soil data, we determined a global map indicating the areas prone for infiltration excess runoff during extreme precipitation events.

Global daily precipitation data were obtained from the Global Precipitation Climatology Centre (GPCC; Schamm et al., 2016). The GPCC dataset contains daily global land-surface precipitation data, interpolated on a regular $1°$ grid for the period 1988-2013. For each grid cell we determined the extreme precipitation (Fig. S2a), defined as the 95th percentile of daily precipitation, considering only rainy days ($>1 \, \mathrm{mm \, day^{-1}}$, Jacob et al., 2014). Infiltration excess runoff is a sub-daily process. While no global sub-daily precipitation data were available, we assumed that 34% of the daily rainfall occurs in the hour with the highest intensity. This fraction we obtained from analysis of hourly precipitation data from 5 precipitation stations within the Segura River catchment covering a period of 25 years (1991-2015). This fraction may vary globally and global extrapolation introduces uncertainty in regions where this fraction differs from our estimate. A higher (lower) fraction may lead to an increase (decrease) of the area prone for infiltration excess surface runoff. Nevertheless, in the absence of better estimates we extrapolated the fraction to illustrate the potential extent of global sensitive areas to infiltration excess runoff.

Infiltration rate was estimated based on the saturated hydraulic conductivity. We obtained global sand, clay and organic matter maps at $10 \, \mathrm{km}$ resolution from the SoilGrids dataset (Hengl et al., 2017). Saturated hydraulic conductivity (Fig. S2b) was obtained by applying pedotransfer functions (Saxton and Rawls, 2006). To obtain an estimate of the infiltration rate we determined the effective saturated hydraulic conductivity K_{eff}. Bouwer (1969) showed that, because of entrapped air, K_{eff} should be smaller than K_{sat} and suggested an approximation of $K_{\mathrm{eff}} \approx 0.5 \, K_{\mathrm{sat}}$.

References

Allen, R. G., Pereira, L., Raes, D., and Smith, M.: Crop evapotranspiration: Guidelines for computing crop requirements, Tech. Rep. 56, FAO, https://doi.org/10.1016/j.eja.2010.12.001, http://www.kimberly.uidaho.edu/water/fao56/fao56.pdf, 1998.

Avendaño-Salas, C., Sanz-Montero, E., Cobo-Rayán, R., and Gómez-Montaña, J. L.: Capacity Situation in Spanish Reservoirs, in: ICOLD, Proceedings of the 19th International Symposium on Large Dams, pp. 849–862, Florence, 1997.

Beven, K. J.: Rainfall-runoff modelling: the primer, John Wiley & Sons, Ltd, Chichester, UK, https://doi.org/10.1002/9781119951001, http://www.scopus.com/inward/record.url?eid=2-s2.0-84888749158{&}partnerID=tZOtx3y1, 2012.

Bouwer, H.: Infiltration of Water into Nonuniform Soil, Journal of the Irrigation and Drainage Division, 95, 451–462, 1969.

Brown, C. B.: Discussion of Sedimentation in reservoirs, Proceedings of the American Society of Civil Engineers, 69, 1493–1500, 1943.

Cerdan, O., Govers, G., Le Bissonnais, Y., Van Oost, K., Poesen, J., Saby, N., Gobin, A., Vacca, A., Quinton, J., Auerswald, K., Klik, A., Kwaad, F. J. P. M., Raclot, D., Ionita, I., Rejman, J., Rousseva, S., Muxart, T., Roxo, M. J., and Dostal, T.: Rates and spatial variations of soil erosion in Europe: A study based on erosion plot data, Geomorphology, 122, 167–177, https://doi.org/10.1016/j.geomorph.2010.06.011, http://dx.doi.org/10.1016/j.geomorph.2010.06.011, 2010.

Eekhout, J. P. C., Terink, W., and de Vente, J.: Assessing the large-scale impacts of environmental change using a coupled hydrology and soil erosion model, Earth Surface Dynamics, 6, 687–703, https://doi.org/10.5194/esurf-6-687-2018, https://www.earth-surf-dynam.net/6/687/2018/, 2018.

Farr, T. G., Rosen, P. A., Caro, E., Crippen, R., Duren, R., Hensley, S., Kobrick, M., Paller, M., Rodriguez, E., Roth, L., Seal, D., Shaffer, S., Shimada, J., Umland, J., Werner, M., Oskin, M., Burbank, D., and Alsdorf, D.: The Shuttle Radar Topography Mission, Reviews of Geophysics, 45, RG2004, https://doi.org/10.1029/2005RG000183, http://doi.wiley.com/10.1029/2005RG000183, 2007.

Heber Green, W. and Ampt, G. A.: Studies on Soil Phyics., The Journal of Agricultural Science, 4, 1–24, https://doi.org/10.1017/S0021859600001441, http://www.journals.cambridge.org/abstract{_}S0021859600001441, 1911.

Hengl, T., Mendes de Jesus, J., Heuvelink, G. B. M., Ruiperez Gonzalez, M., Kilibarda, M., Blagotić, A., Shangguan, W., Wright, M. N., Geng, X., Bauer-Marschallinger, B., Guevara, M. A., Vargas, R., MacMillan, R. A., Batjes, N. H., Leenaars, J. G. B., Ribeiro, E., Wheeler, I., Mantel, S., and Kempen, B.: SoilGrids250m: Global gridded soil information based on machine learning, PLOS ONE, 12, e0169 748, https://doi.org/10.1371/journal.pone.0169748, http://dx.plos.org/10.1371/journal.pone.0169748https://dx.plos.org/10.1371/journal.pone.0169748, 2017.

Jacob, D., Petersen, J., Eggert, B., Alias, A., Christensen, O. B., Bouwer, L. M., Braun, A., Colette, A., Déqué, M., Georgievski, G., Georgopoulou, E., Gobiet, A., Menut, L., Nikulin, G., Haensler, A., Hempelmann, N., Jones, C., Keuler, K., Kovats, S., Kröner, N., Kotlarski, S., Kriegsmann, A., Martin, E., van Meijgaard, E., Moseley, C., Pfeifer, S., Preuschmann, S., Radermacher, C., Radtke, K., Rechid, D., Rounsevell, M., Samuelsson, P., Somot, S., Soussana, J.-F., Teichmann, C., Valentini, R., Vautard, R., Weber, B., and Yiou, P.: EURO-CORDEX: new high-resolution climate change projections for European impact research, Regional Environmental Change, 14, 563–578, https://doi.org/10.1007/s10113-013-0499-2, http://link.springer.com/10.1007/s10113-013-0499-2http://download.springer.com/static/pdf/221/art:10.1007/s10113-013-0499-2.pdf?originUrl=http://link.springer.com/article/10.1007/s10113-013-0499-2{&}token2=exp=1462793760{~}acl=/static/pdf/221/art:10.1007/s10, 2014.

Maetens, W., Vanmaercke, M., Poesen, J., Jankauskas, B., Jankauskiene, G., and Ionita, I.: Effects of land use on annual runoff and soil loss in Europe and the Mediterranean: A meta-analysis of plot data, Progress in Physical Geography, 36, 599–653, https://doi.org/10.1177/0309133312451303, http://ppg.sagepub.com/cgi/doi/10.1177/0309133312451303, 2012.

MAPAMA: Mapa de Cultivos y Aprovechamientos de España 2000-2010 (1: 50.000), http://www.magrama.gob.es/es/cartografia-y-sig/publicaciones/agricultura/mac{_}2000{_}2009.aspx, 2010.

Morgan, R. P. C. and Duzant, J. H.: Modified MMF (Morgan–Morgan–Finney) model for evaluating effects of crops and vegetation cover on soil erosion, Earth Surface Processes and Landforms, 33, 90–106, https://doi.org/10.1002/esp.1530, http://doi.wiley.com/10.1002/esp.1530, 2008.

Nash, J. E. and Sutcliffe, J. V.: River Flow Forecasting Through Conceptual Models Part I-a Discussion of Principles*, Journal of Hydrology, 10, 282–290, https://doi.org/10.1016/0022-1694(70)90255-6, 1970.

Poesen, J. W., van Wesemael, B., Bunte, K., and Benet, A. S.: Variation of rock fragment cover and size along semiarid hillslopes: a case-study from southeast Spain, Geomorphology, 23, 323–335, https://doi.org/10.1016/S0169-555X(98)00013-0, http://linkinghub.elsevier.com/retrieve/pii/S0169555X98000130, 1998.

Prosser, I. P. and Rustomji, P.: Sediment transport capacity relations for overland flow, Progress in Physical Geography, 24, 179–193, https://doi.org/10.1177/030913330002400202, http://ppg.sagepub.com/content/24/2/179.full.pdfhttp://ppg.sagepub.com/cgi/doi/10.1177/030913330002400202, 2000.

Quansah, C.: Laboratory experimentation for the statistical derivation of equations for soil erosion modelling and soil conservation design, Ph.D. thesis, Cranfield Institute of Technology, http://ethos.bl.uk/OrderDetails.do?uin=uk.bl.ethos.337734, 1982.

Saxton, K. E. and Rawls, W. J.: Soil Water Characteristic Estimates by Texture and Organic Matter for Hydrologic Solutions, Soil Science Society of America Journal, 70, 1569, https://doi.org/10.2136/sssaj2005.0117, https://www.soils.org/publications/sssaj/abstracts/70/5/1569, 2006.

Schamm, K., Ziese, M., Raykova, K., Becker, A., Finger, P., Meyer-Christoffer, A., and Schneider, U.: GPCC Full Data Daily Version 1.0: Daily Land-Surface Precipitation from Rain Gauges built on GTS based and Historic Data, https://doi.org/10.5065/D6V69GRT, https://doi.org/10.5065/D6V69GRT, 2016.

Sellers, P. J., Tucker, C. J., Collatz, G. J., Los, S. O., Justice, C. O., Dazlich, D. A., and Randall, D. A.: A Revised Land Surface Parameterization (SiB2) for Atmospheric GCMS. Part II: The Generation of Global Fields of Terrestrial Biophysical Parameters from Satellite Data, Journal of Climate, 9, 706–737, https://doi.org/10.1175/1520-0442(1996)009<0706:ARLSPF>2.0.CO;2, http://journals.ametsoc.org/doi/abs/10.1175/1520-0442(1996)009{%}3C0706:ARLSPF{%}3E2.0.CO;2, 1996.

Terink, W., Lutz, A. F., Simons, G. W. H., Immerzeel, W. W., and Droogers, P.: SPHY v2.0: Spatial Processes in HYdrology, Geoscientific Model Development, 8, 2009–2034, https://doi.org/10.5194/gmd-8-2009-2015, http://www.geosci-model-dev.net/8/2009/2015/, 2015.

Tollner, E. W., Barfield, B. J., Haan, C. T., and Kao, T. Y.: Suspended Sediment Filtration Capacity of Simulated Vegetation, Transactions of the ASAE, 19, 0678–0682, https://doi.org/10.13031/2013.36095, http://elibrary.asabe.org/abstract.asp??JID=3{&}AID=36095{&}CID=t1976{&}v=19{&}i=4{&}T=1, 1976.

Venables, W. N. and Ripley, B. D.: Modern Applied Statistics with S, Springer, New York, fourth edi edn., 2002.
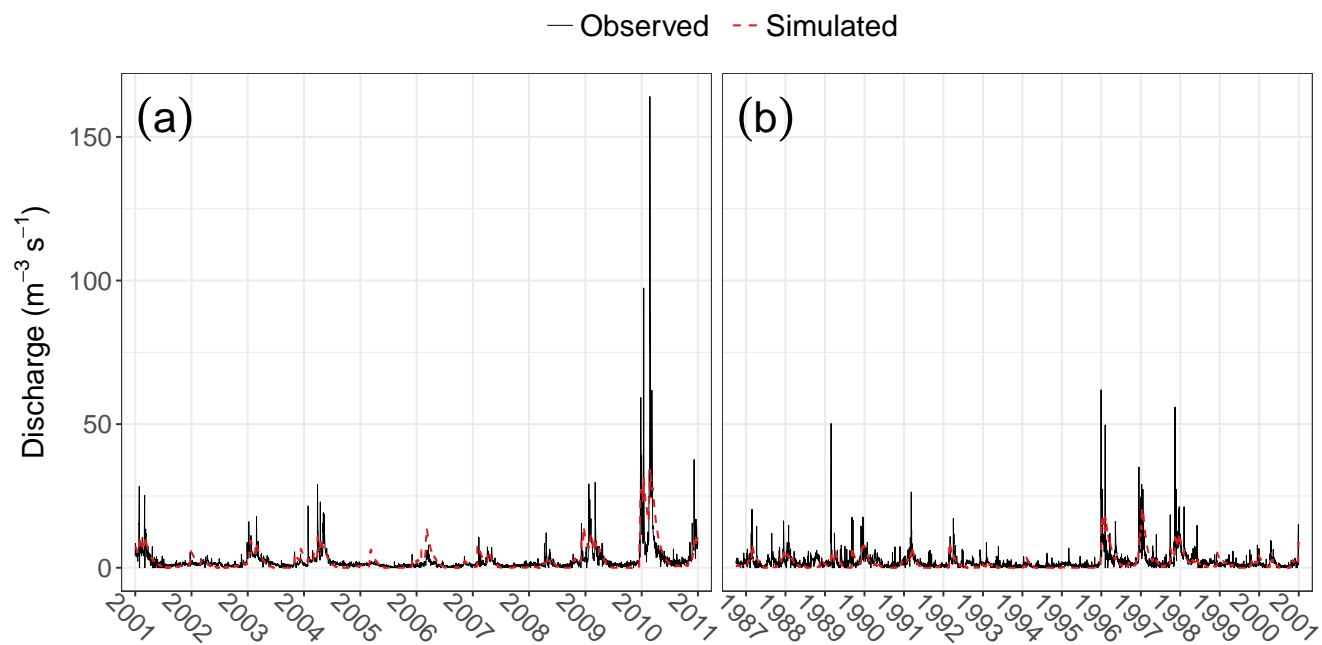
Figure S1. Discharge time series for the calibration (a) and validation period (b). The dashed red line correspond to the simulated time series and the solid black line corresponds to the observed time series.
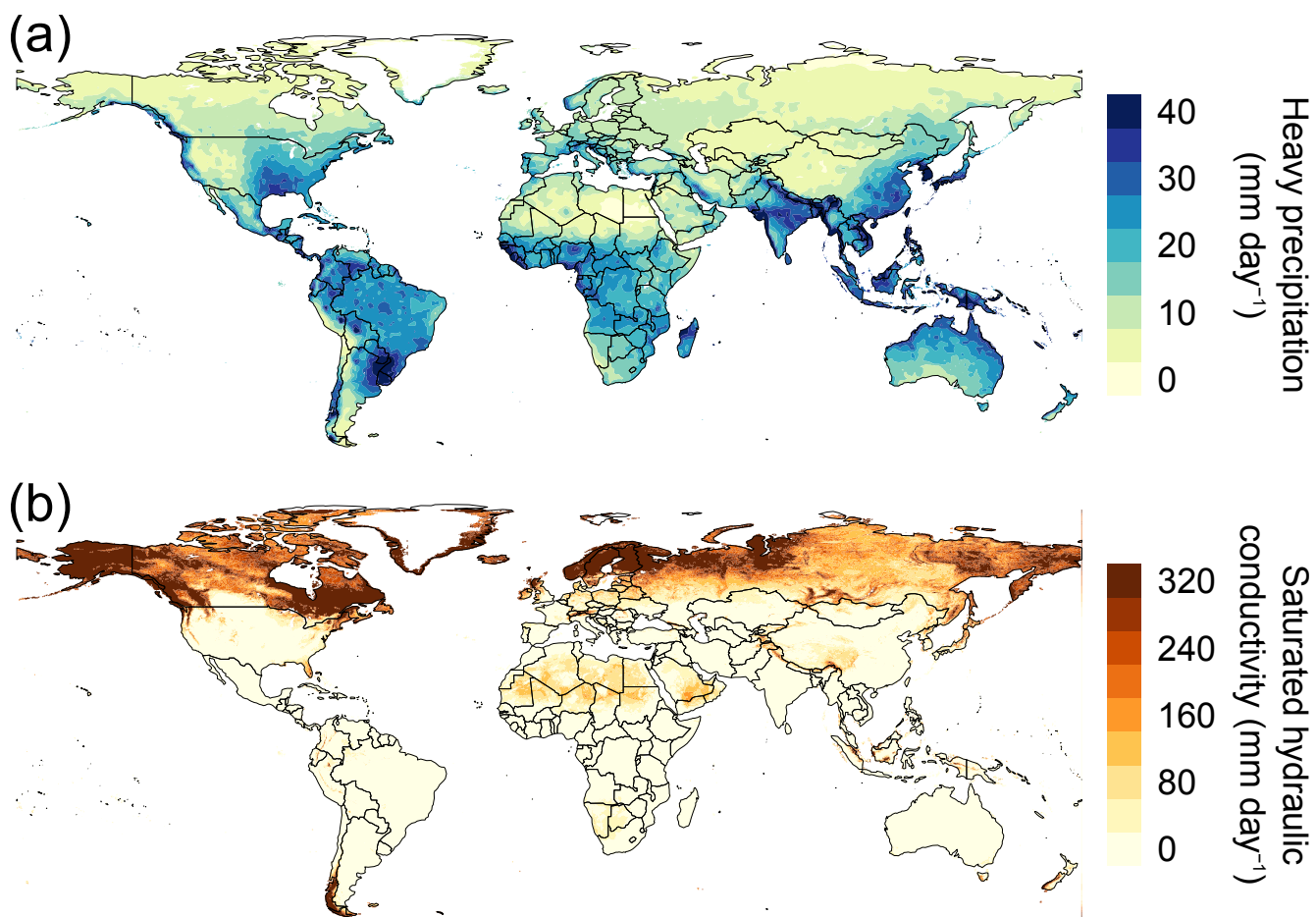
Figure S2. (a) Global heavy precipitation $(\mathrm{mm\,day^{-1}})$ and (b) global saturated hydraulic conductivity map $(\mathrm{mm\,day^{-1}})$.
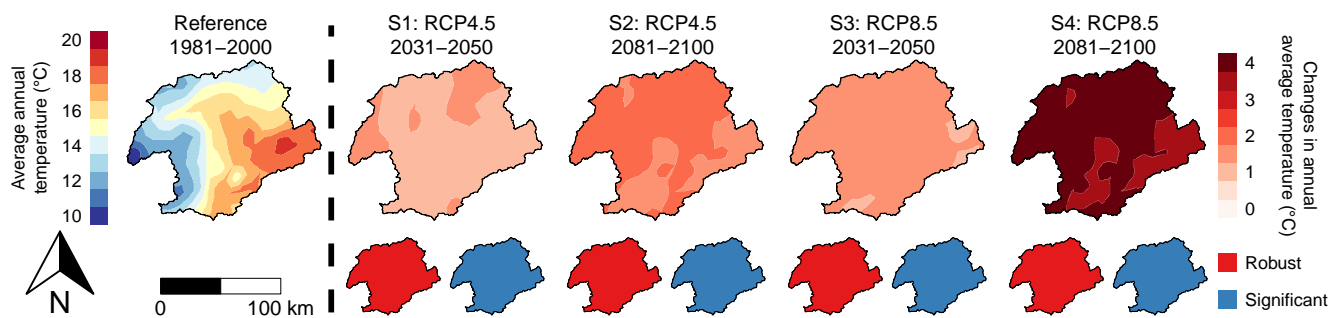
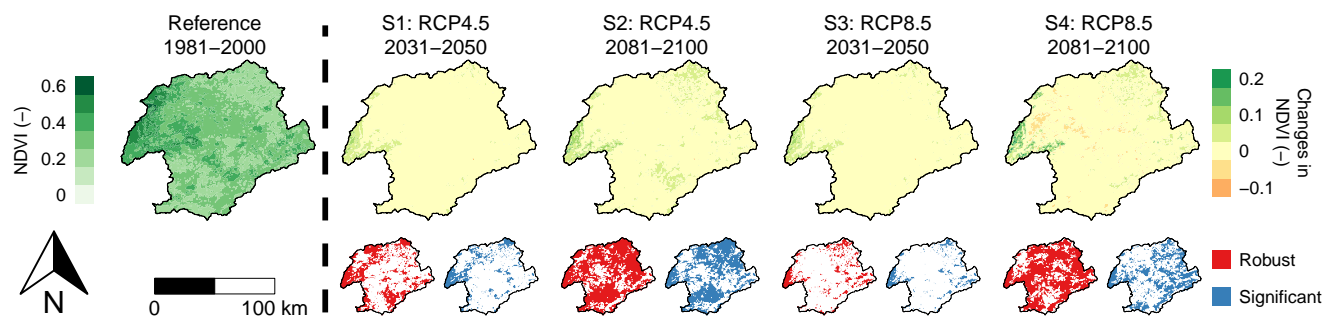**Figure S3.** Ensemble average annual-average temperature (°C) for the reference scenario (left) and changes between the reference scenario and the four future scenarios (right).
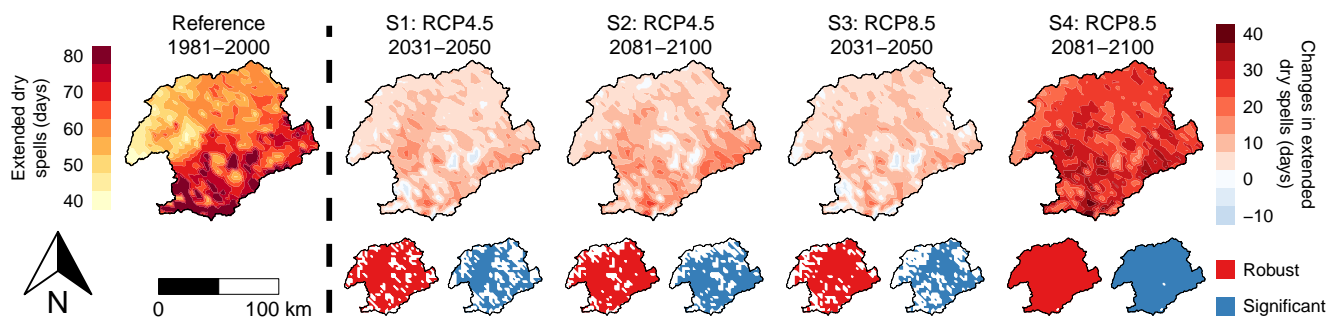
**Figure S4.** Ensemble average dry spells (days) defined as the 95th percentile of the duration of periods of at least 5 consecutive days with daily precipitation below 1 mm, for the reference scenario (left) and changes between the reference scenario and the four future scenarios (right).

Figure S5. Ensemble average NDVI (-) for the reference scenario (left) and changes between the reference scenario and the four future scenarios (right).
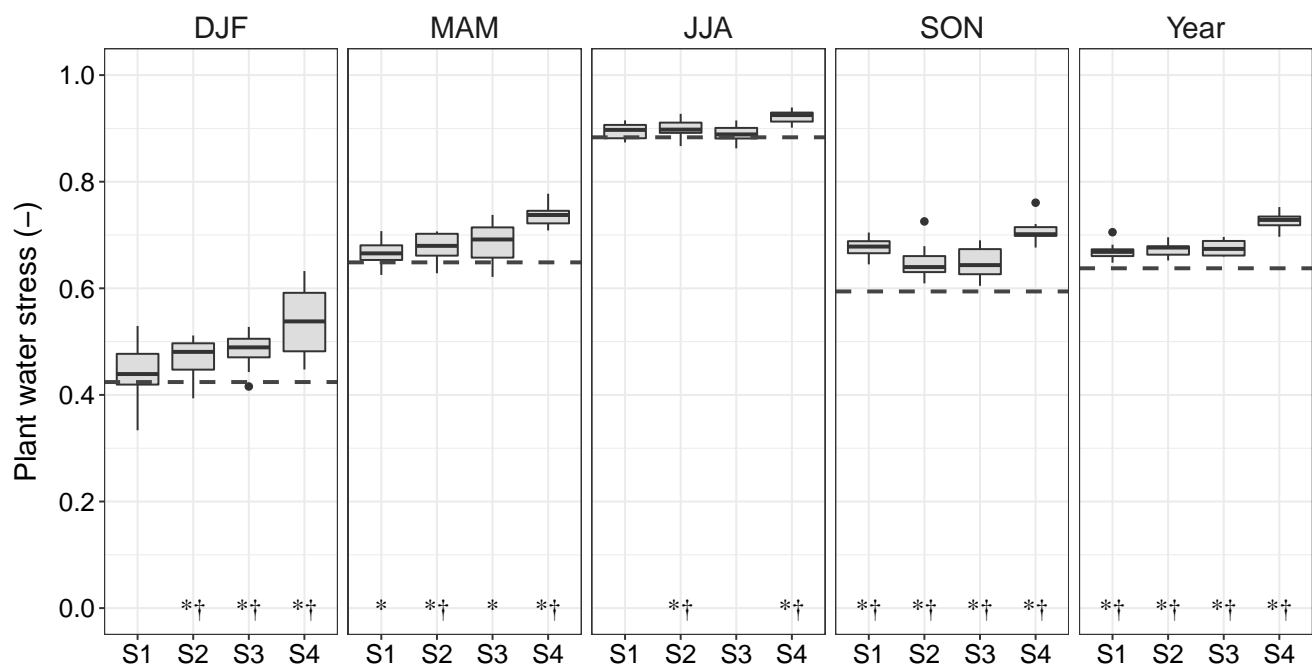
Figure S6. Catchment-average plant water stress (-), averaged by season: winter (DJF), spring (MAM), summer (JJA), autumn (SON), and for the whole year. The boxplots indicate the spread of the catchment-average among the nine climate models. In each panel the horizontal dashed line represents the catchment-average value for the reference scenario. An asterisk (∗) indicates a robust change and a dagger (†) indicates a significant change (p<0.05). The boxplots are described as follows: the hinges indicate the 25th and 75th percentiles, the thick horizontal line indicates the median, the whiskers indicate 1.5 times the inter quantile range from each of the two hinges and the dots indicate outliers.
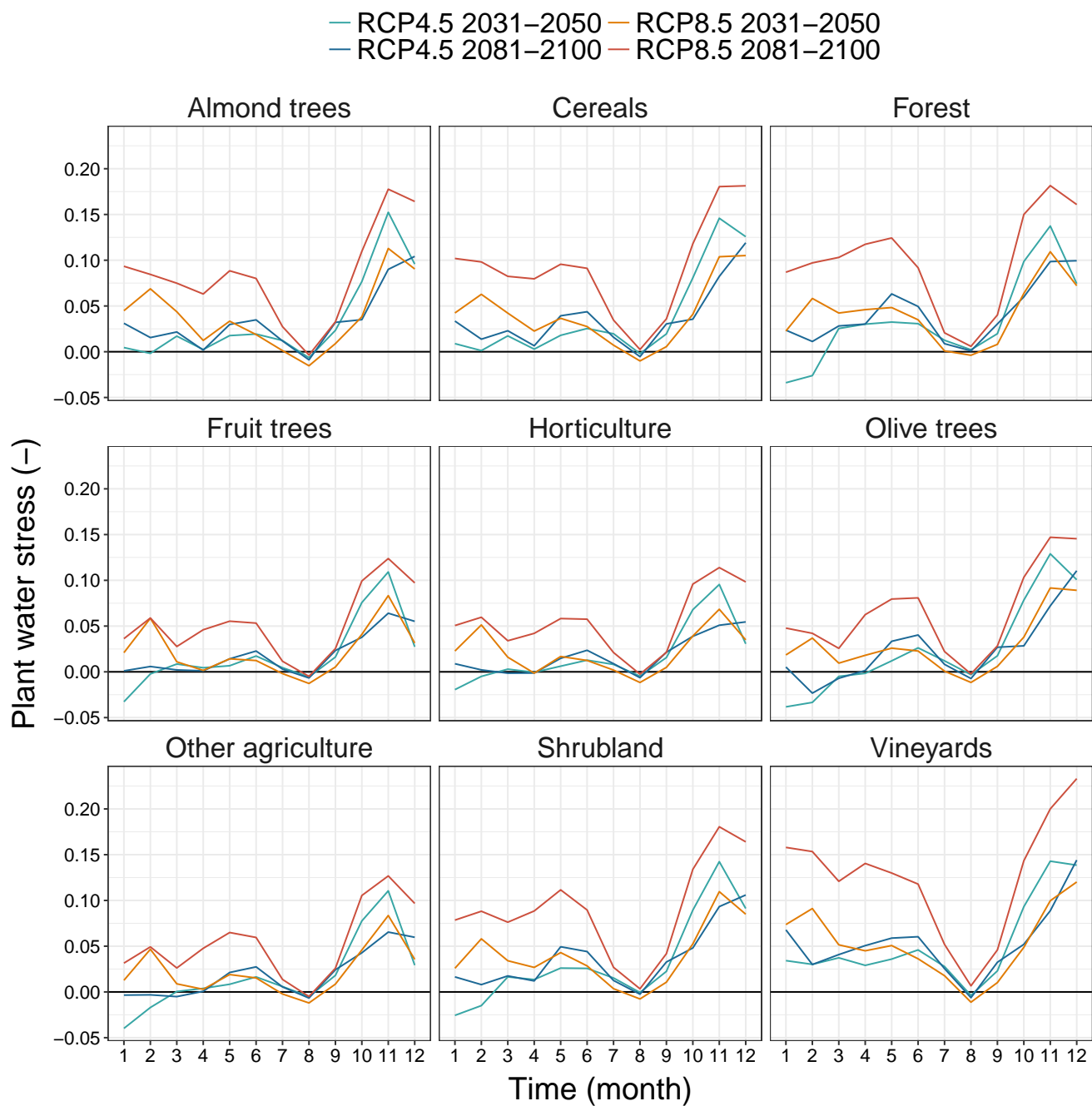
Figure S7. Monthly average plant water stress (-) per landuse class. The plant water stress is shown as a difference with respect to the reference scenario.
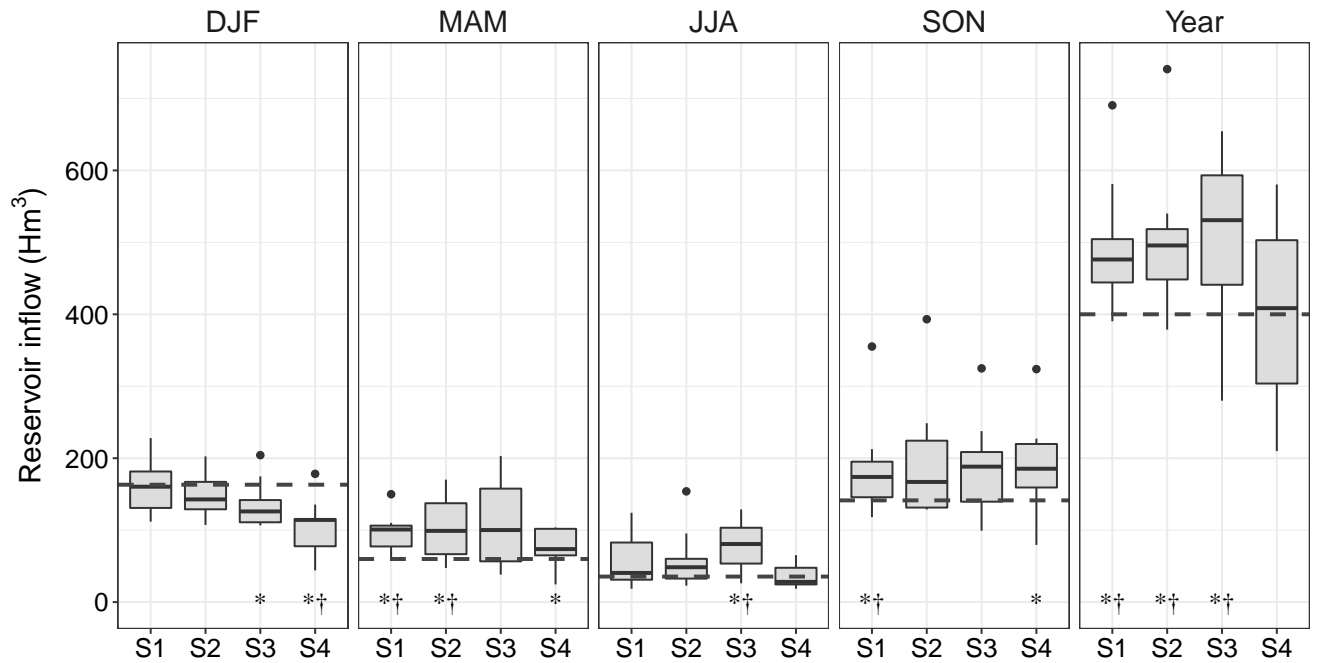
Figure S8. Catchment-average reservoir inflow (Hm^3), averaged by season: winter (DJF), spring (MAM), summer (JJA), autumn (SON), and for the whole year. The boxplots indicate the spread of the catchment-average among the nine climate models. In each panel the horizontal dashed line represents the catchment-average value for the reference scenario. An asterisk (∗) indicates a robust change and a dagger (†) indicates a significant change (p<0.05). The boxplots are described as follows: the hinges indicate the 25th and 75th percentiles, the thick horizontal line indicates the median, the whiskers indicate 1.5 times the inter quantile range from each of the two hinges and the dots indicate outliers.
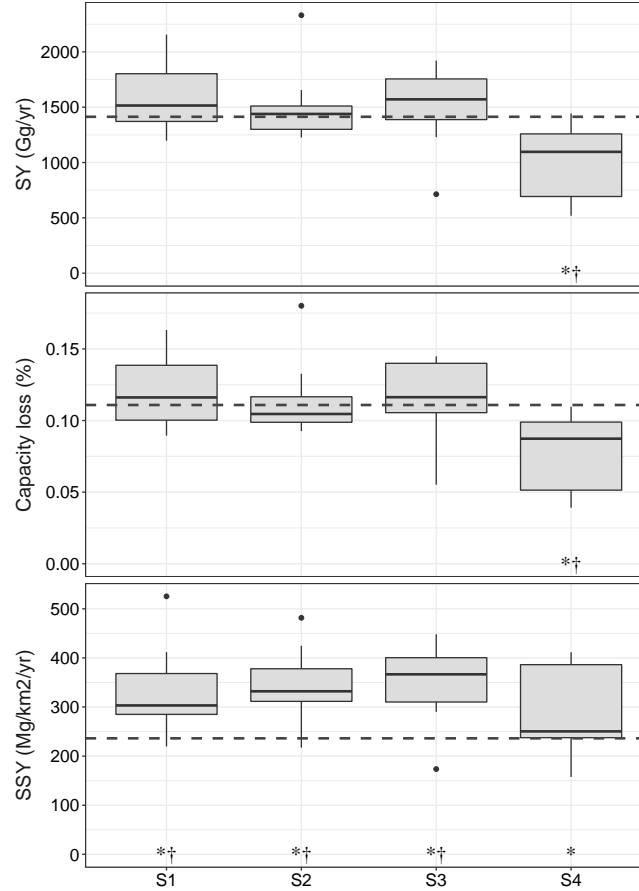
Figure S9. Catchment-average reservoir sediment yield (SY) ($Gg\,yr^{-1}$), capacity loss (%) and hillslope erosion (SSY) ($Mg\,km^{-2}\,yr^{-1}$). The boxplots indicate the spread of the catchment-average among the nine climate models. In each panel the horizontal dashed line represents the catchment-average value for the reference scenario. An asterisk ($*$) indicates a robust change and a dagger ($\dagger$) indicates a significant change ($p<0.05$). The boxplots are described as follows: the hinges indicate the 25th and 75th percentiles, the thick horizontal line indicates the median, the whiskers indicate 1.5 times the inter quantile range from each of the two hinges and the dots indicate outliers.

Table S1. Overview of the parameters that were used to calibrate the hydrological model.

Acronym	Description	Units	Calibrated value	Parameter range
CapRiseMax	Maximum capillary rise	mm	2	0-10
RootDryFrac	Fraction of the permanent wilting point (rootzone)	-	0	0-2
Alpha	Fraction of daily rainfall that occurs in the hour with the highest intensity	-	0.34	0-1
Labda_infil	Infiltration excess parameter	-	0.25	0-1
DeltaGw	Groundwater recharge delay time	day	500	0-500
NDVImax	Maximum NDVI	-	0.65	0-1
NDVImin	Minimum NDVI	-	0.1	0-1
Kcmax	Maximum crop coefficient	-	1.5	0-1.5
Kcmin	Minimum crop coefficient	-	0.5	0-1.5
kx	Flow recession coefficient	-	0.973	0-0.999

Table S2. The name and capacity of the 14 reservoirs considered in this study. The reservoir number corresponds to the numbers in Fig. 1b.

nr	name	capacity (Hm^3)
1	Taibilla	9
2	Fuensanta	210
3	Talave	35
4	Cenajo	437
5	Camarillas	36
6	Argos	10
7	Alfonso XIII	22
8	La Cierva	7
9	Valdeinfierno	13
10	Puentes	26
11	Algeciras	45
12	Ojós	1
13	Mayes	2
14	Crevillente	13

Table S3. The nine climate models used in this study, with their corresponding RCM, GCM and research institute.

RCM GCM	CCLM[a]	HIRHAM5[b]	RACMO[c]	RCA[d]	WRF[e]
CNRM-CM5	X			X	
EC-EARTH	X	X	X	X	
IPSL-CM5A-MR					X
MPI-ESM-LR	X			X	

[a] Climate Limited-area Modelling-Community (CLMcom), [b] Danish Meteorological Institute (DMI), [c] Royal Netherlands Meteorological Institute (KNMI), [d] Swedish Meteorological and Hydrological Institute (SMHI), [e] Institut Pierre Simon Laplace (IPSL)

Table S4. Catchment-average change of the water security indicators. Values for the reference scenario are presented in absolute values. All other values are differences with respect to the reference scenario and are accompanied with percentages in parentheses. Values marked in bolt are significantly different ($p < 0.05$).

scenario	period	plant water stress (-)	hillslope erosion ($\mathrm{Mg\,km^{-2}\,yr^{-1}}$)	reservoir inflow ($\mathrm{Hm^3}$)	sediment yield ($\mathrm{Gg\,yr^{-1}}$)	capacity loss (%)
reference	1981-2000	0.64	227.3	400.0	1082.4	0.11
RCP 4.5	2031-2050	**0.03 (5.2)**	**89.0 (39.1)**	**99.6 (24.9)**	88.6 (8.2)	0.01 (8.5)
RCP 4.5	2081-2100	**0.04 (5.6)**	**101.4 (44.6)**	**103.9 (26.0)**	43.9 (4.1)	0.00 (4.4)
RCP 8.5	2031-2050	**0.04 (5.9)**	**104.2 (45.9)**	**111.7 (27.9)**	39.8 (3.7)	0.00 (4.0)
RCP 8.5	2081-2100	**0.09 (13.7)**	53.5 (23.5)	1.1 (0.3)	**-352.6 (-32.6)**	**-0.04 (-32.2)**

Table S5. Catchment-average change of hydrological indicators. Values for the reference scenario are presented in absolute values. All other values are differences with respect to the reference scenario and are accompanied with percentages in parentheses. Values marked in bolt are significantly different ($p < 0.05$).

scenario	period	precipitation (mm)	actual evapotranspiration (mm)	surface runoff (mm)	infiltration (mm)	soil moisture content (mm)
reference	1981-2000	361.5	314.2	38.0	262.9	11.6
RCP 4.5	2031-2050	-8.0 (-2.2)	**-19.4 (-6.2)**	14.9 (39.1)	**-13.7 (-5.2)**	-0.8 (-6.6)
RCP 4.5	2081-2100	-3.5 (-1.0)	-16.9 (-5.4)	**19.1 (50.2)**	-11.9 (-4.5)	**-1.1 (-9.9)**
RCP 8.5	2031-2050	-8.9 (-2.4)	-21.8 (-6.9)	**19.0 (50.0)**	-16.8 (-6.4)	**-1.2 (-10.5)**
RCP 8.5	2081-2100	**-65.2 (-18.0)**	**-66.6 (-21.2)**	12.8 (33.6)	**-57.6 (-21.9)**	**-3.3 (-28.6)**